Synthetic Metals 321 (2026) 118263

Contents lists available at ScienceDirect

Synthetic Metals

journal homepage: www.elsevier.com/locate/synmet

Tuning electromagnetic absorption for EMI shielding in PBSA composites with Fe_3O_4-decorated carbon nanotubes

Artis Krikovs [a,*], Miks Bleija [a,*], Oskars Platnieks [a], Dzmitry Tsyhanok [b], Juras Banys [b], Jan Macutkevič [b], Krisjanis Smits [c], Mikhail Maiorov [d], Sergejs Gaidukovs [a,e]

[a] Institute of Chemistry and Chemical Technology, Faculty of Natural Sciences and Technology, Riga Technical University (RTU), P. Valdena 3, Riga LV-1048, Latvia
[b] Institute of Applied Electrodynamics and Telecommunications, Physics faculty, Vilnius University (VU), Sauletekio ave. 3, Vilnius LT-10257, Lithuania
[c] Institute of Biomaterials and Bioengineering, Faculty of Natural Sciences and Technology, Riga Technical University, Riga LV-1048, Latvia
[d] Institute of Physics, University of Latvia, Miera 32, Salaspils LV-2169, Latvia
[e] Department of Materials Science and Engineering, Korea University, Seoul 02841, Republic of Korea

ARTICLE INFO

Keywords:
Poly(butylene succinate-co-adipate)
Electrical percolation
Impedance matching
Conductive-magnetic hybrid nanofillers
Biodegradable polyester
Aqueous co-precipitation

ABSTRACT

This study investigates the electromagnetic interference (EMI) shielding behavior of bio-based poly(butylene succinate-co-adipate) (PBSA) composites filled with magnetite (Fe_3O_4)-grafted single-walled (SWCNT) and multi-walled carbon nanotubes (MWCNT). Hybrid fillers were synthesized via one-step aqueous co-precipitation onto non-functionalized CNTs, yielding nominal Fe_3O_4 contents of 15 and 30 wt% (actual: 12.1–26.9 wt%), expressed as a fraction of the total filler mass. They were then incorporated into PBSA at 0.10–2.0 vol% via solvent casting. Microscopy revealed two distinct hybrid filler morphologies: individual Fe_3O_4 nanoparticles dispersed along CNT sidewalls and agglomerates concentrated at CNT junctions. Magnetometry showed that the deposited Fe_3O_4 was superparamagnetic, with specific magnetization calculated to range from 4.7 to 65 emu/g depending on crystallite size. Tensile testing revealed up to a 2.2-fold increase in elastic modulus and a 1.4-fold increase in ultimate tensile strength. Sheet resistance indicated percolation at ~ 0.1 vol%, increasing to ~ 0.5 vol % after Fe_3O_4 co-precipitation. The composites were analyzed by electromagnetic spectroscopy in the frequency ranges of 0.1–3 GHz and 8.4–12.6 GHz. CNT incorporation produced shielding in which dissipation carried the larger share of the shielding effectiveness, with $\langle SE_A \rangle / \langle SE_T \rangle$ ratios of up to 0.78. Fe_3O_4-grafted MWCNT composites at 1.0 vol% exhibited a broadband absorption plateau below 3 GHz ($\langle SE_A \rangle / \langle SE_T \rangle$ ratio of 0.70), which the SWCNT-based composites did not develop in this range. Unmodified SWCNT composites at 2.0 vol% transitioned to reflection-dominated shielding at 8.4–12.6 GHz. This work indicates that CNT morphology is an important design variable for absorption-based EMI shielding.

1. Introduction

Electromagnetic interference (EMI) shielding materials are required wherever densely packed electronic components must operate without mutual disturbance [1]. As device architectures move toward higher integration density and higher operating frequencies, the relevant bands become increasingly congested [2–4], and in the 1–6 GHz range device emissions overlap with wireless communication bands [5–7]. This motivates shielding materials that are simultaneously lightweight, thin, and effective [8]. Polymer composites are attractive in this context because their effective intrinsic impedance can be tuned toward the free-space value ($\eta_0 = 377\ \Omega$) through filler selection, in contrast to metals, whose shielding is dominated by front-surface reflection [9,10]. Throughout this work, the frequency-resolved total shielding effectiveness in decibels is written as $SE_T(f) = SE_R(f) + SE_A(f)$, where $SE_R(f)$ and $SE_A(f)$ are the reflection and absorption contributions to the loss. Independently of these dB quantities, the incident power is partitioned into reflected, transmitted, and absorbed fractions $R(f)$, $T(f)$, and $A(f) = 1 - R(f) - T(f)$, obtained from the measured complex scattering parameters. Any description of a composite as predominantly "absorbing" or "reflecting" refers explicitly to this *RA* power balance rather than to $SE_A(f)$ alone.

Carbon nanotubes (CNTs) form percolating conductive networks at very low loadings, typically 0.1–1 vol% depending on length, aspect

* Corresponding authors.
E-mail addresses: artis.krikovs@rtu.lv (A. Krikovs), miks.bleija@rtu.lv (M. Bleija), sergejs.gaidukovs@rtu.lv (S. Gaidukovs).

https://doi.org/10.1016/j.synthmet.2026.118263
Received 11 May 2026; Received in revised form 21 July 2026; Accepted 2 August 2026
Available online 4 August 2026
0379-6779/© 2026 The Author(s). Published by Elsevier B.V. This is an open access article under the CC BY license (http://creativecommons.org/licenses/by/4.0/).

ratio, and dispersion [11–15]. The delocalized electrons of CNTs raise the complex permittivity and the associated dielectric loss, which is the principal loss mechanism in these systems [16]. Other carbon fillers such as graphene nanoplatelets (GNP) provide comparable effects at higher loadings, e.g., Zeranska et al. used up to 10 wt% GNP in acrylonitrile-butadiene-styrene [4]. The main motivation for CNT selection in this work was increasing their effectiveness at markedly lower filler contents.

A purely conductive filler network favors reflection-dominated shielding, since impedance mismatch grows with electrical conductivity [17]. The impedance mismatch due to the high electrical conductivity (and complex permittivity loss) increases shielding effectiveness by reflection. However, the aim is to increase the absorption and to reduce the effects of stray and reflected EM radiation as interference. This can be accomplished by the addition of magnetic fillers such as carbonyl iron, magnetite (Fe_3O_4), and soft ferrites. Magnetic fillers raise permeability and permeability loss μ'', reducing the impedance mismatch that arises from purely dielectric loading, and contribute to absorption through natural ferromagnetic resonance, eddy-current loss, and domain-wall resonance, which together raise μ'' [11,18–20].

Theoretically, EM propagation within a lossy medium is governed by the complex propagation constant [21]:

$$\gamma = \alpha + j\beta = j\omega\sqrt{\mu\varepsilon}\sqrt{1 - j\frac{\sigma}{\omega\varepsilon}}, \quad (1)$$

where ω is the angular frequency, σ is the electrical conductivity, ε is the dielectric permittivity, μ is the magnetic permeability, α is the attenuation constant, $\beta = 2\pi/\lambda$ is the phase change constant, and λ is the operating wavelength in the medium. And in a lossy medium the characteristic wave impedance η is complex:

$$\eta = \frac{j\omega\mu}{\gamma} \quad (2)$$

Absorption can be maximized by increasing both permittivity and permeability losses, while maintaining the impedance matching.

Recent advances show that a useful strategy to approach the impedance/loss problem is a combination of both magnetic and electrical structural components above the percolation threshold, in the form of surface functionalized nanocarbon [22,23]. Saeed et al. first generated Fe_2O_3-polyethylene glycol nanoparticles, then grew a Fe_3O_4 shell on them before decorating functionalized MWCNTs with Fe_2O_3/-Fe_3O_4 clusters [11]. Yu et al. employed nitric-acid functionalization followed by an ultrasonication-assisted hydrothermal growth of Fe oxides on CNTs, with subsequent washing and re-processing under varied ultrasonication times to obtain mixed α-Fe_2O_3/Fe_3O_4/CNT phases, effectively a two-stage modification [24]. Wang et al. use ferrocene in benzene in a single solvothermal step at 500 °C to form Fe_3O_4-CNT nanocomposites, requiring an autoclave and organometallic precursors [25]. Sadegh et al. use a two-stage route, first synthesizing Fe_3O_4 nanoparticles by chemical coprecipitation and then decorating nitric-acid-functionalized MWCNTs [26]. Dai et al. prepared low-reflection carboxymethyl-cellulose/MWCNT@Fe_3O_4 films by depositing high Fe_3O_4 loadings onto acid-functionalized MWCNTs and assembling the resulting hybrids via vacuum filtration, yielding ultrathin, flexible EMI shielding films [27]. A relatively similar route to the present work was reported by Wei et al., who deposited ultra-small Fe_3O_4 onto non-functionalized MWCNTs through repeated aqueous coprecipitation cycles and then used cationic-surfactant-assisted latex mixing to form segregated networks in natural rubber [18]. The co-precipitation procedure employed in this study was adapted from previously reported methods and is not intended as a novel synthesis approach. Instead, a simplified single-batch route was applied consistently to both SWCNTs and MWCNTs, providing a unified preparation platform to investigate the influence of CNT wall structure and Fe_3O_4 distribution on the resulting PBSA composite properties.

Beyond synthesis, recent studies show that the spatial organization of Fe_3O_4 on CNTs is an important structural factor controlling EMI shielding and absorption behavior. Wei et al. showed that ultra-small Fe_3O_4 nanoparticles anchored on non-functionalized MWCNTs can preserve a conductive CNT network while introducing magnetic and polarization-loss sites, improving impedance matching and reducing front-surface reflection [18]. Dai et al. further showed that increasing the Fe_3O_4 coating degree on MWCNTs in carboxymethyl-cellulose films decreases electrical conductivity but increases magnetization, leading to a lower reflection coefficient and higher absorbed power fraction [27]. These results indicate that Fe_3O_4 distribution on CNTs is not only a synthesis-related feature, but also a structure-property parameter that affects conductive network formation, impedance matching, and absorption-oriented EMI shielding behavior.

Decorating CNT surfaces is not the only way to achieve strong hybrid interactions. For example, Lee et al. integrated MWCNT, graphene, and Fe_3O_4 into tricontinuous networks in a block-copolymer matrix, where one block preferentially interacts with Fe_3O_4 and the other with the CNT/graphene network, yielding co-assembled conductive magnetic domains that differ from the single hybrid filler approach discussed above [28]. Dispersion quality also strongly affects performance, since van der Waals and magnetic dipole-dipole interactions promote clustering, which solution sonication and solvent casting are used to mitigate [29–31].

Most reported shielding composites use non-degradable, petroleum-derived matrices. Among biodegradable alternatives, polylactic acid (PLA) is the most studied [32–35], whereas softer aliphatic polyesters remain relatively underexplored. Poly(butylene succinate-co-adipate) (PBSA) was selected here for multiple reasons in addition to its sustainability: it is a flexible, film-forming, biodegradable, and partially bio-based copolyester whose ductility helps offset CNT-induced stiffening and embrittlement and enables thin free-standing films, while its polar ester groups may contribute to the dielectric response at low loadings [36–38]. Unlike the more rigid poly(3-hydroxybutyrate) (PHB) and PLA, PBSA is a ductile, fully aliphatic platform that is far less investigated for EMI shielding than PLA [39], rubber [18], polyurethane [40], cellulose-derived matrices [27], or epoxy [41].

Despite considerable progress in the development of CNT-based magnetic nanocomposites, several key questions remain unresolved for low-loading biodegradable and bio-based polyester systems. It is unclear how the wall structure of carbon nanotubes (single- versus multi-walled) influences the nucleation, distribution, and agglomeration of Fe_3O_4 nanoparticles on the CNT surface, which is investigated through the morphological and structural characterization presented in this work. The effect of these differences in hybrid nanofiller architecture on the formation of conductive networks and the resulting electrical conductivity and impedance matching of PBSA composites has not been systematically examined. Also, it remains unknown whether Fe_3O_4 functionalization shifts the EMI shielding mechanism from reflection-dominated to absorption-dominated behavior, and how this transition depends on the CNT structure and magnetic filler loading. These questions are addressed through a combined analysis of nanofiller morphology, electrical conductivity, magnetic properties, and EMI shielding performance.

In this study, a simplified one-step aqueous co-precipitation method is employed to graft Fe_3O_4 onto non-functionalized SWCNTs and MWCNTs, avoiding prior chemical functionalization and multi-step processing. The resulting hybrid fillers are incorporated into a bio-based PBSA matrix to systematically investigate the effects of CNT type, Fe_3O_4 content, and filler loading on electrical, electromagnetic, thermal, mechanical, and rheological properties. We evaluate whether Fe_3O_4 modification promotes absorption-based EMI shielding.

2. Experimental

2.1. Materials

All the materials used in this work are available commercially. Poly (butylene succinate-co-adipate) (PBSA) FD92PM pellets were purchased from PTT MCC Biochem Co., Ltd., (Bangkok, Thailand). PBSA is a semi-crystalline thermoplastic polyester with a nominal density of 1.24 g/cm^3 (manufacturer); measured 1.227 g/cm^3 (this work) and MFI of 4 g/10 min (190 °C, 2.16 kg). It is completely biodegradable and partially bio-based (20–50%, DIN CERTCO 8C083). Multi-walled carbon nanotubes (MWCNT) NC7000 were purchased from Nanocyl SA, (Sambreville, Belgium; purity >90 wt%). Single-walled carbon nanotubes (SWCNT) TUBALL were purchased from OCSiAl Europe S.a.r.l. (Leudelange, Luxembourg; purity >80 wt%). Chloroform (≥ 99%), laboratory-grade NaOH, $FeCl_2{\cdot}4H_2O$, and $FeCl_3{\cdot}6H_2O$ were purchased from Merck KGaA, (Darmstadt, Germany). PBSA pellets were dried in a vacuum oven (J.P. Selecta, Barcelona, Spain) before use according to the manufacturer's recommendation (70 °C, 24 h). Carbon nanotubes were used as received without any further purification and were stored in sealed packaging.

2.2. Synthesis and sample preparation

2.2.1. CNT-g-Fe_3O_4 synthesis

Grafted CNTs (MWCNT-g-Fe_3O_4 and SWCNT-g-Fe_3O_4) with a Fe_3O_4 content of 15 and 30 wt% were prepared as follows: 3.5 g of CNTs were weighed and dispersed in 700 mL of water and sonicated using an ultrasonic sonotrode Hielscher UIS250V (Hielscher Ultrasonics GmbH, Teltow, Germany) operating at 250 W and duty cycle of 0.7 for 30 min. The suspension was transferred to a three-necked round-bottom flask with a magnetic stir bar, with a septum in the first neck, a loose glass stopper in the second neck, and a gas inlet capillary affixed in the third neck with several layers of parafilm. The suspension was purged with N_2 for 30 min to remove dissolved oxygen and saturate the solution with N_2, while stirring over a magnetic stir plate. Afterwards, 0.53 and 1.29 g of $FeCl_2{\cdot}4H_2O$, and 1.44 and 3.50 g of $FeCl_3{\cdot}6H_2O$, (Fe^{3+} and Fe^{2+} in a 2:1 stoichiometric mol/mol ratio) were quickly added to the flask, and the glass stopper was affixed with parafilm. The mass of reagents was weighed accordingly to produce a final CNT-*g*-Fe_3O_4 with a Fe_3O_4 content of 15 and 30 wt% respectively. The solution was stirred for an additional 30 min to dissolve the salts. A NaOH solution containing the stoichiometric amount of NaOH (8 OH^- per formula unit of Fe_3O_4; 0.85 g and 2.07 g for the 15 and 30 wt% batches, respectively), with an additional excess to reach basic pH, was added dropwise over a 30-minute period using a syringe, while maintaining an inert atmosphere.

The co-precipitation can be described by the following reaction [42]:

$$CNT + Fe^{2+} + \quad 2Fe^{3+} + \quad 8OH^- \rightarrow CNT\ g\ Fe_3O_4 + 4H_2O$$

The solution was heated to 60 °C and stirred for 2 h. Afterwards, the obtained product was filtered, washed with water and ethanol, and dried in a vacuum oven at 60 °C for 24 h. The product was then used to prepare the nanocomposites.

For brevity, the Fe_3O_4-grafted MWCNT variants with 15 wt% and 30 wt% Fe_3O_4 are denoted 15MF and 30MF, respectively; the corresponding SWCNT variants are denoted 15SF and 30SF. The neat MWCNT and SWCNT are denoted MW and SW, respectively.

2.2.2. Composite preparation

The nanocomposites were prepared via a solvent-casting process. Nanoparticles were dispersed in 200 mL of chloroform using an ultrasonic sonotrode (250 W, 0.7 cycle), in combination with a mechanical overhead mixer at 1000 RPM and a water bath for cooling for 45 min. Afterwards, PBSA pellets were dissolved in chloroform (12 g /100 mL) and combined with the nanoparticle dispersion. The mixture was homogenized using the overhead mixer at 1000 RPM and heated at 62 °C for two hours to improve filler dispersion, reduce the probability of filler settling out of solution, and evaporate solvent. The final solution (about 150 mL) was cast in a Petri dish in a fume hood and left to evaporate overnight. Any leftover solvent was removed by vacuum drying (24 h at 70 °C). The filler weight (wt%) and volume (vol%) fractions of the produced systems can be seen in the supplementary Table S3. The initial MW samples were prepared with an incorrect calculation of the filler volume fraction; however, this discrepancy has been accounted for within the reported results.

To obtain defined sample dimensions, compression molding (135 °C, 5 min) (Carver Inc., Wabash, OH, USA) between steel plates, followed by rapid cooling to room temperature (21 °C), was used, with the thickness set by the molding frame. Films and sheets with nominal thicknesses of 100 μm, 400 μm, 500 μm, and 700 μm were prepared. Sample thickness was matched to the requirements of each characterization method rather than varied as a study variable: 100 μm films for four-point sheet resistance, 400 μm for broadband dielectric spectroscopy, dynamic mechanical analysis, and tensile testing, 500 μm for the waveguide measurements, and 700 μm for light flash analysis. Nominal frame thicknesses are reported throughout; where the evaluation of a measurement required the sample thickness, the individually measured value of the specimen was used.

2.3. Characterization

2.3.1. Nanofiller XRD

X-ray diffraction analysis was done on Rigaku Ultima + with a sealed Cu anode tube (Cu Kα radiation). XRD provides crystal phase identification and quantitative phase analysis. Measurements were conducted with scanning speed of 2 °/min, at 40 kV voltage and 5 mA amperage. Diffraction data was acquired in 2θ angle range from 5 ° to 80 °. For data analysis MDI Jade Standard L−2 A (2025) program was used. For phase identification and quantitative analysis ICDD (PDF−5 + 2025) database was used by comparing acquired diffractogram maxima with the database.

2.3.2. Nanofiller TGA and Fe_3O_4 content determination

The Fe_3O_4 content of the CNT-Fe_3O_4 hybrid nanofillers was determined by thermogravimetric analysis (TGA) using a TG50 (Mettler-Toledo, Switzerland). Each nanofiller was heated from 25 to 950 °C at a heating rate of 20 °C min^{-1} in air atmosphere (30 mL min^{-1}). After reaching 950 °C, the samples were held isothermally for 30 min to ensure complete oxidation of the carbon nanotubes. The remaining species were considered as an α-Fe_2O_3 phase.

Because commercial CNTs contain residual metallic catalyst particles originating from their synthesis, pristine CNTs were analyzed under identical conditions to quantify the mass of the residual inorganic impurities. The deposited Fe_3O_4 mass fraction x of each hybrid nanofiller was obtained from the residual mass balance, residue $= (1 - x){\cdot}r_{CNT} + 1.0345{\cdot}x$, where r_{CNT} is the residue of the corresponding pristine CNT measured under identical conditions and 1.0345 is the mass gain of the Fe_3O_4 to Fe_2O_3 conversion.

The obtained Fe_2O_3 mass was subsequently converted to the equivalent Fe_3O_4 content using the stoichiometric relationship between Fe_2O_3 and Fe_3O_4.

2.3.3. Nanofiller VSM

The saturation magnetization (M_s), remanent magnetization (M_r), and coercivity (H_c) of the materials were measured at room temperature using a vibrating sample magnetometer (VSM, Lake Shore Cryotronic Co., model 7404, USA). The measurements were performed with cyclic changes of the magnetic field in the range from −10 kOe to + 10 kOe, with saturation values reported at 10 kOe.

Pristine MWCNT and SWCNT were measured under identical conditions to determine the contribution of the residual growth catalyst.

2.3.4. Nanofiller STEM

The morphology of prepared nanoparticles was analyzed by scanning transmission electron microscopy (STEM) Thermo Fisher Scientific Verios 5 XHR (Eindhoven, The Netherlands). The images were generated using transmitted electrons at an acceleration voltage of 40 kV. Nanoparticle samples were produced by extreme dilution and ultrasonication, followed by microdrop deposition on a holey-carbon film as the conductive substrate.

2.3.5. Composite fracture surface SEM

The morphology of the composite fracture surfaces was analyzed by scanning electron microscopy (SEM) Verios 5 XHR SEM (Verios, Thermo Scientific, USA). The images were generated using backscattered electrons (CBS detector) at an acceleration voltage of 30 kV.

2.3.6. Composite density

The densities of the composites were determined using the hydrostatic displacement method by measuring sample weights in air and ethanol ($d_{EtOH} = 0.805$ g/cm^3) with a Sartorius KBBA 100 (Sartorius AG, Göttingen, Germany) analytical balance equipped with a Sartorius YDK 01 hydrostatic density measurement kit. The density [d_{EX} (g/cm^3)] was calculated according to the manufacturer's protocol:

$$d_{EX} = \frac{m_a(d_{EtOH} - 0.0012)}{0.99983(m_a - m_s)} + 0.0012, \quad (3)$$

where m_a (g) is the sample's mass in air, m_s is the sample's apparent mass as measured when submerged in ethanol (g), and d_{EtOH} is the density of ethanol (0.805 g/cm^3), which was determined with a hydrometer. The measured values are shown in the supplementary Table S3.

2.3.7. Four-point sheet resistance

The sheet resistance of the PBSA composites was measured using Signatone S−302–4 a four-point probe system (Signatone Corporation, Gilroy, CA, USA) in combination with a Keithley 2450 source measure unit (Keithley Instruments, LLC., Cleveland, OH, USA). Square films with a thickness of 100 μm and a side length of 60 mm were tested over a current range of 10 nA to 10 mA, with a maximum voltage of 21 V, until a stable resistance value was reached. Each measurement was repeated at least five times per sample. Sheet resistance was then calculated according to the manufacturer's guidelines provided by Signatone:

$$R_s = 4.5324 \frac{U}{I} f_1 f_2, \quad (4)$$

where R_s is the electrical sheet resistance (Ωsq^{-1}), 4.5324 is the correction factor determined by the model of the four-point probe, according to the technical data by Signatone, U is the measured voltage (V), I is the applied current (A), f_1 is the correction factor for the sample thickness, and f_2 is the correction factor for the sample geometry ($f_2 = 1$ as the probe spacing is magnitudes of order smaller than the sample size).

The correction factor for sample thickness was calculated as follows:

$$f_1 = \frac{\ln(2)}{\ln\left[\frac{\sinh(\frac{t}{s})}{\sinh(\frac{t}{2s})}\right]}, \quad (5)$$

where t is the thickness of the sample (100 μm), and s is the probe spacing (1000 μm).

2.3.8. Broadband dielectric spectroscopy

In the frequency range from 10 Hz to 40 MHz at room temperature, the AC conductivity [σ' (Sm^{-1})] was measured using a Novocontrol BDS 50 broadband dielectric spectrometer (Novocontrol Technologies GmbH & Co. KG, Montabaur, Germany). Composite disks with a diameter of 30 mm and a thickness of 400 μm were coated with silver-filled copper conductive paint (843AR Super Shield, M. G. Chemicals Ltd., Burlington, ON, Canada) to minimize contact resistance and were placed between plate electrodes to form a capacitive cell.

The electrical conductivity and sheet resistance percolation thresholds of the composites were approximated according to the classic percolation theory [43,44] and the following equations [45]:

$$\sigma = \sigma_0(vol. - vol._p)^t \quad (6)$$

$$R_s = R_{s0}(vol. - vol._p)^p, \quad (7)$$

where R_s (Ωsq^{-1}) is the sheet resistance, σ (Sm^{-1}) is the volume conductivity at 10 Hz, R_{s0} and σ_0 are the proportionality coefficients, $vol.$ is the filler concentration, $vol._p$ is the percolation threshold, and t and p are the critical exponents. The values of $vol._p$ were approximated by minimizing the R^2 value residuals of the fits.

2.3.9. Electromagnetic shielding and absorption

An Agilent 8714ET vector network analyzer (Agilent Technologies Inc., Santa Clara, CA, USA) was used for measurements in the frequency range 0.1–3 GHz. In this frequency range the complex dielectric permittivity was determined from complex reflectivity data.

In the microwave frequency range of 8.4–12.6 GHz a waveguide spectrometer was used. Samples with a thickness of 0.5 mm were placed in a waveguide holder, and the complex dielectric permittivity was calculated according to the literature [46]. The reflection, transmission, and absorption reported in Section 3.5 were computed for a 1 mm layer from the measured complex permittivity using Eqs. 11 and 12.

2.3.10. Differential scanning calorimetry

Differential scanning calorimetry (DSC) measurements were performed on a DSC−1 instrument (Mettler-Toledo, Switzerland) under nitrogen atmosphere. Samples of approximately 10 mg were tested in standard aluminum pans and analyzed over a temperature range of −50–140 °C at heating/cooling rate of 10 °C min^{-1}. The degree of crystallinity of the PBSA composites was calculated from the melting peaks using eq.

$$\chi_c = \frac{\Delta H_m}{\Delta H_m^0 w_f}, \quad (8)$$

where ΔH_m is the melting enthalpy of composite, ΔH_m^0 is the melting enthalpy for 100% crystalline PBSA and is taken as 110.3 J/g [47], and w_f is the mass fraction of PBSA.

2.3.11. Light flash analysis

The thermal dissipative properties of the composites were measured using a NETZSCH LFA 447 NanoFlash light flash analysis apparatus (NETZSCH-Gerätebau GmbH, Selb, Germany) equipped with a standard 12.7 mm sample holder for through-plane diffusivity measurements according to ISO 22007–4. Square samples were coated with a Graphit 33 graphite spray, following the manufacturer's recommendations, to ensure uniform surface absorptivity and comparability with reference standards. Thermal conductivity was calculated using the equation:

$$\lambda(T) = \alpha(T)\,\rho(T) C_p(T), \quad (9)$$

where λ is thermal conductivity ($Wm^{-1}K^{-1}$), α is diffusivity (mm^2s^{-1}), ρ is density ($g\,cm^{-3}$) C_p is specific heat capacity (Jg^{-1} K^{-1}).

LFA measures sample diffusivity according to the half-time method:

$$\alpha = \frac{0.1388 d^2}{t_{\frac{1}{2}}}, \quad (10)$$

where d is the sample thickness (700 μm), and $t_{\frac{1}{2}}$ is the half-rise time of the IR detector signal.

Due to the highly insulating nature of polymer composites, the

adiabatic model was not applicable; instead, the Cowan model [48] provided by the LFA analysis software was used as the most suitable approach. Sample-specific heat capacities were determined using the same software via comparison with a reference material of known heat capacity. All measurements were conducted at 25 °C. Each sample was measured five times consecutively, with a 120 s interval between measurements to ensure thermal equilibration. Considering uncertainties in specific heat capacity determination, density and sample thickness, the overall accuracy of the thermal conductivity measurements was estimated to be within ± 0.02 $Wm^{-1} K^{-1}$.

2.3.12. Thermogravimetric analysis

Thermal stability was measured by thermogravimetric analysis using a TG50 (Mettler-Toledo, Switzerland) in air atmosphere at a heating rate of 10 °C min^{-1} in temperature range of 25–800 °C.

2.3.13. Oscillatory rheology

Polymer composite melt rheology was measured using Anton Paar SmartPave 102 (Graz, Austria). A parallel plate measuring system with 25 mm diameter and a fixed temperature of 140 °C was used. Oscillatory measurements were registered at an angular frequency range of 0.1–100 rad s^{-1} and fixed strain amplitude of 1%.

2.3.14. Dynamical mechanical analysis

Dynamic mechanical analysis was performed using dynamic mechanical analyzer DMA/SDTA861e (Mettler-Toledo, Switzerland). Measurements were conducted using a small tensile clamping assembly, in a temperature range of −60–70 °C, at heating rate of 3 °C min^{-1}, applied force of 5 N, displacement amplitude of 10 μm and frequency of 1 Hz. Tests samples were cut out of compression-molded films with a thickness of 400 μm.

2.3.15. Tensile testing

Tensile properties were measured using a Tinius Olsen Model 25ST universal testing machine. Testing was conducted at a crosshead speed of 2 mm min^{-1} up to 2% strain, followed by 20 mm min^{-1} until fracture. Samples with width of 10 mm and a thickness of 0.4 mm were cut from compression-molded films, and paper tape tabs were attached to the ends to prevent slippage. The gauge length was set to 45 mm. The elastic modulus was determined from the linear region of the stress-strain curve within a strain range of 0.2–0.5%. Yield strength (σ_y) and yield strain (ε_y) were defined as the maximum in the stress-strain curve.

3. Results and discussion

3.1. Nanofiller characterization

3.1.1. X-ray diffraction analysis of prepared nanofillers

The XRD patterns of samples (a)30MF and 15MF, and (b)30SF and 15SF are shown in Fig. 1, with standard JCPDS cards included for comparison (Card Nos. 019–0629 (Fe_3O_4) and 058–1638 (CNT)). Broad diffraction bands at 2θ 24–26 ° and ~ 43 ° are observed in all samples and are assigned to the crystallographic planes (002) and (100) directions of CNTs, respectively [49]. The Fe_3O_4 (400) peak at 2θ ≈ 43 ° overlaps with the CNT (100) reflection; assignment in this region is ambiguous and relies on the presence of the non-overlapping (220), (311), (511), and (440) peaks at 30 °, 35 °, 57 °, and 63 ° [49]. The results match well with the characteristic peaks of Fe_3O_4 from standard JCPDS card, confirming its successful nanoparticle deposition on the surface of the CNTs.

In Fig. 1a, 15MF Fe_3O_4 peaks are weaker and significantly broader compared to the 30MF sample. Similarly in Fig. 1b, 15SF Fe_3O_4 peaks are less distinguishable compared to 30SF, due to lower loading of Fe_3O_4. The SWCNT (002) reflection is more intense than the MWCNT equivalent due to the higher graphitic order of the SWCNT bundle lattice [50], which reduces the relative contrast of the Fe_3O_4 reflections against the carbon background. In addition, MF showed more pronounced peak broadening compared to SF. Such broadening is associated with nanoscale crystallite size and lattice strain effects, as described by the Scherrer relation and related models [51,52]. Scherrer analysis of the (311) plane reflection yielded crystallite sizes of ~2.9 and ~5.7 nm for 15MF and 30MF, respectively, whereas 15SF and 30SF showed larger crystallite sizes of ~7.5 and ~7.9 nm, respectively. However, due to the noisy diffraction curves, the crystallite sizes are expected to be very variable. Similar reductions in Fe_3O_4 peak intensity have been reported in CNT/Fe_3O_4 composites due to the dominance of the carbon phase [53].

3.1.2. TGA of nanofillers

Fe_3O_4 nanoparticle content in decorated CNTs was determined by TGA, and the results are shown in Table 1 and Figure S1. After the isothermal hold in air, the residual weight fractions of the 15MF, 30MF, 15SF, and 30SF hybrids were 18.9%, 33.2%, 29.4%, and 38.2%, respectively, with 7.3% for the neat MWCNT and 18.5% for the neat SWCNT. The neat-SWCNT residue corresponds to the encapsulated iron catalyst reported for this product [54] and equals 12.9 wt% iron after conversion from Fe_2O_3. Fe_3O_4 oxidizes to Fe_2O_3 in air below the carbon combustion range [55], so the hybrid residue was treated as Fe_2O_3 originating from both the deposited Fe_3O_4 and the CNT-borne catalyst. The deposited Fe_3O_4 mass fraction was obtained from the mass balance

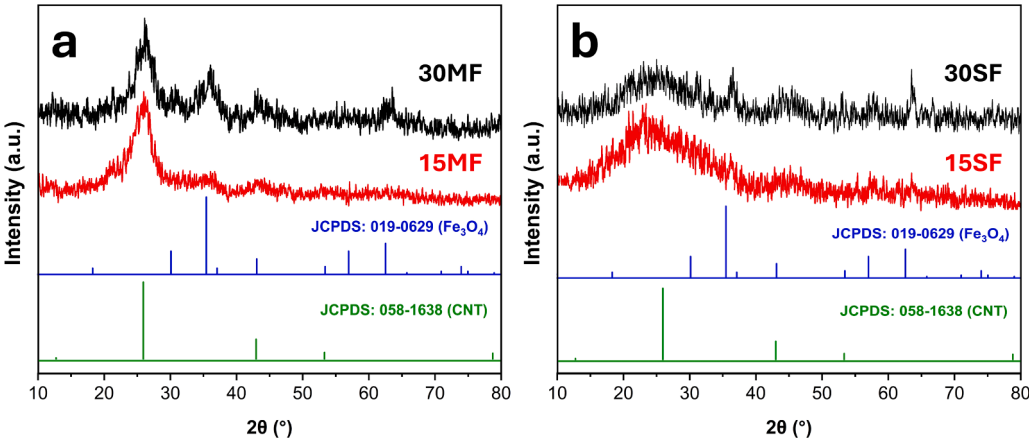

Fig. 1. XRD patterns of modified CNTs: (a) 30MF and 15MF, and (b) 30SF and 15SF, with corresponding JCPDS cards (019–0629 and 058–1638).

Table 1
TGA residual mass and deposited Fe_3O_4 content of nanofillers.

Material	Ash weight (%)*	Fe_3O_4 weight (%)
MWCNT	7.3	-
15MF	18.9	12.1
30MF	33.2	26.9
SWCNT	18.5	-
15SF	29.4	12.8
30SF	38.2	23.2

* Ash weight normalized to dry weight of the samples (remaining mass at 110°C)

Table 2
Magnetization data.

Sample	M_s (emu/g)	M_r (emu/g)	M_r/M_s	H_c (Oe)
MWCNT	0.62	0.09	0.14	65
15MF	1.1	0.12	0.11	74
30MF	4.2	0.10	0.03	12
SWCNT	17.2	0.95	0.06	25
15SF	21.0	1.29	0.06	20
30SF	28.3	2.49	0.09	40

(Section 2.3.2). This gives deposited Fe_3O_4 loadings of 12.1%, 26.9%, 12.8%, and 23.2% in 15MF, 30MF, 15SF, and 30SF, respectively, corresponding to 77–86% of the nominal 15 and 30 wt% targets.

3.1.3. VSM analysis of prepared nanofillers

Room temperature magnetization data for the four hybrid nanofillers are shown in Fig. 2 and Table 2. The magnetization at 10 kOe (M_s) reached 1.11 and 4.18 emu/g for 15MF and 30MF, and 21.0 and 28.3 emu/g for 15SF and 30SF, increasing with Fe_3O_4 content in both series. All four samples showed weak hysteresis, with coercivities of 12–74 Oe and remanence-to-M_s ratios of 0.025–0.108. The largest coercivity, 74 Oe, occurred for 15MF, which also showed the lowest M_s.

The magnetic response of the hybrids contains a contribution from the residual growth catalyst of the CNTs, which was measured directly on the pristine nanotubes (Fig. 2, Table 2). Neat SWCNT reaches 17.2 emu/g at 10 kOe with a coercivity of 25 Oe. Related to its catalyst iron content of 12.9 wt% (Section 3.1.2), this corresponds to 134 emu per gram of iron, at the bulk cementite value of 128–140 emu/g and well below metallic iron (218 emu/g) [56], consistent with encapsulated carbide and size-reduced metallic particles [57]. Neat MWCNT reaches 0.62 emu/g with a coercivity of 65 Oe, reflecting its smaller, alumina-supported catalyst residue (7.3 wt%). Relative to the hybrid magnetization at 10 kOe, the catalyst accounts for 49% in 15MF, 11% in 30MF, 72% in 15SF, and 47% in 30SF.

With the catalyst contribution measured directly, the specific magnetization of the deposited oxide follows separately for each hybrid from $M_{hybrid} = (1-x) \bullet M_{CNT} + x \bullet M_{oxide}$, where x is the deposited Fe_3O_4 fraction from the TGA mass balance (Table 1) and M_{CNT} is the pristine-CNT value; we assume that the carbon-encapsulated catalyst is unaltered by the aqueous co-precipitation. The deposited oxide reaches 4.7 and 13.9 emu/g in 15MF and 30MF and 47 and 65 emu/g in 15SF and 30SF, with a sensitivity of ±0.4 to ±2.5 emu/g to a ± 1 wt% uncertainty in x. The oxide magnetization increases monotonically with the XRD crystallite size across all four samples (2.9, 5.7, 7.5, and 7.9 nm; Section 3.1.1). The SWCNT-grown oxide reaches 51–70% of the bulk Fe_3O_4 value of 92 emu/g [58], while the MWCNT-grown oxide remains at 5–15%. Expressed as bulk-Fe_3O_4 equivalent, the deposited oxide corresponds to 0.6, 4.1, 6.5, and 16.3 wt% of hybrid mass, against the 12.1–26.9 wt% total deposited oxide from TGA, which provides an estimate of the magnetically inactive or disordered fraction. The reduction relative to bulk follows the behavior of few-nanometer Fe_3O_4, where surface spin disorder and incomplete crystallization suppress the net moment, and non-magnetic species such as FeO(OH) and Fe_2O_3 formed during co-precipitation may contribute to the deficit, particularly in the MWCNT series.

The coercivity trends reflect the relative contributions of the catalyst residue and deposited Fe_3O_4 rather than particle size alone. For 15MF, where the catalyst accounts for approximately 49% of the total magnetization, the coercivity (74 Oe) remains close to that of the neat MWCNTs (65 Oe), suggesting that the magnetic response is still largely influenced by the catalyst residue. In contrast, for 30MF, where the Fe_3O_4 contribution increases to 89% of the total magnetization, the coercivity decreases to 12 Oe, consistent with the predominantly superparamagnetic behavior of the 5.7 nm Fe_3O_4 nanoparticles. The SWCNT series remains dominated by the catalyst contribution, with coercivities of 25 Oe for neat SWCNTs and 20 Oe for 15SF. The higher coercivity observed for 30SF (40 Oe), which also exhibited the greatest degree of Fe_3O_4 agglomeration (Section 3.1.4), may be associated with increased dipolar interactions between closely spaced particles, resulting in a higher effective magnetic anisotropy, although this mechanism cannot be confirmed from the present measurements. The low remanence ratios (0.03–0.14) observed for all samples indicate that only a small fraction of the magnetic particles remains thermally blocked at room temperature, consistent with the measured Fe_3O_4 crystallite sizes of 3–8 nm, which are well below the reported superparamagnetic threshold of approximately 20 nm for co-precipitated Fe_3O_4 [59].

3.1.4. Nanofiller STEM

STEM micrographs of Fe_3O_4-grafted CNT nanofillers are presented in Fig. 3. The light grey network corresponds to CNTs, while dark/black spots represent Fe_3O_4 nanoparticles and their agglomerates. Fe_3O_4 particles are observed on both MWCNT and SWCNT surfaces, appearing either as individual dispersed nanoparticles or as agglomerates of varying sizes. The red circles highlight regions where individual Fe_3O_4 nanoparticles are attached to the CNT surface. Prepared Fe_3O_4

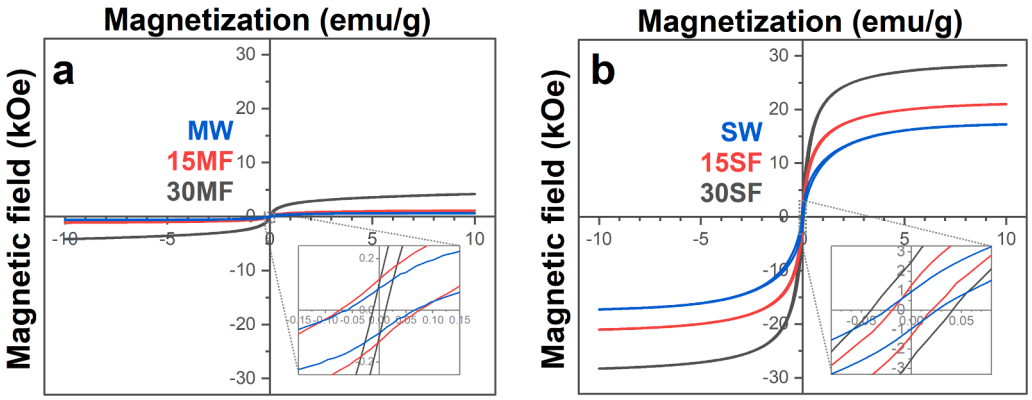

Fig. 2. VSM measurements of CNTs: (a) MW, 15MF and 30MF, and (b) SW, 15SF and 30SF.

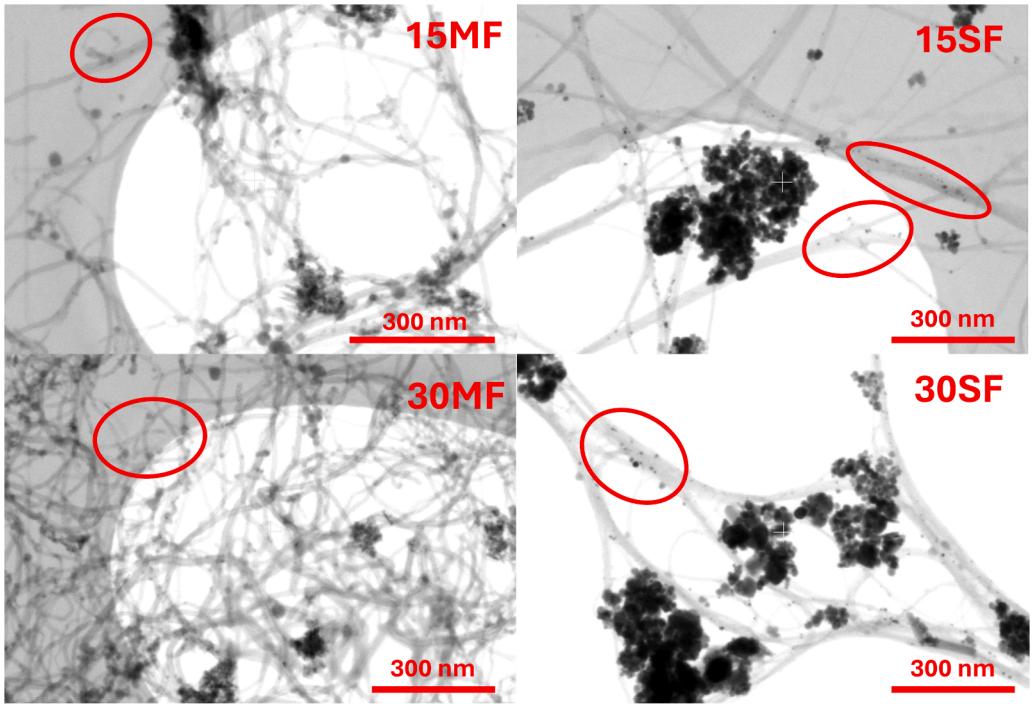

Fig. 3. STEM micrographs of 15MF, 30MF, 15SF, and 30SF nanofillers. Red circles highlight individual Fe_3O_4 nanoparticles.

nanoparticles have a diameter of approximately 10 nm. At lower Fe_3O_4 loading (15MF and 15SF), nanoparticles are well dispersed along nanotubes, with fewer agglomerates, but increasing the Fe_3O_4 concentration promotes the formation of agglomerates. The 30SF sample exhibits pronounced agglomeration, indicating reduced dispersion at higher Fe_3O_4 content. In supplementary information, a lower magnification micrograph (Figure S2) shows distribution of larger agglomerates along with their size variations in the range of 50–550 nm. Similar size variations were reported by Zhong et al., who chemically functionalized CNTs and deposited Fe_3O_4 nanoparticles via an in situ co-precipitation process, yielding nanoparticles of ~10 nm and agglomerates larger than 100 nm on the surface of the modified CNTs [60]. Elemental mapping of the composites was attempted by EDS, but at the dilute overall iron content the Fe signal could not be resolved above background, so the particle and agglomerate size assignments rest on the STEM contrast, the XRD crystallite sizes (Section 3.1.1), and the magnetization analysis (Section 3.1.3).

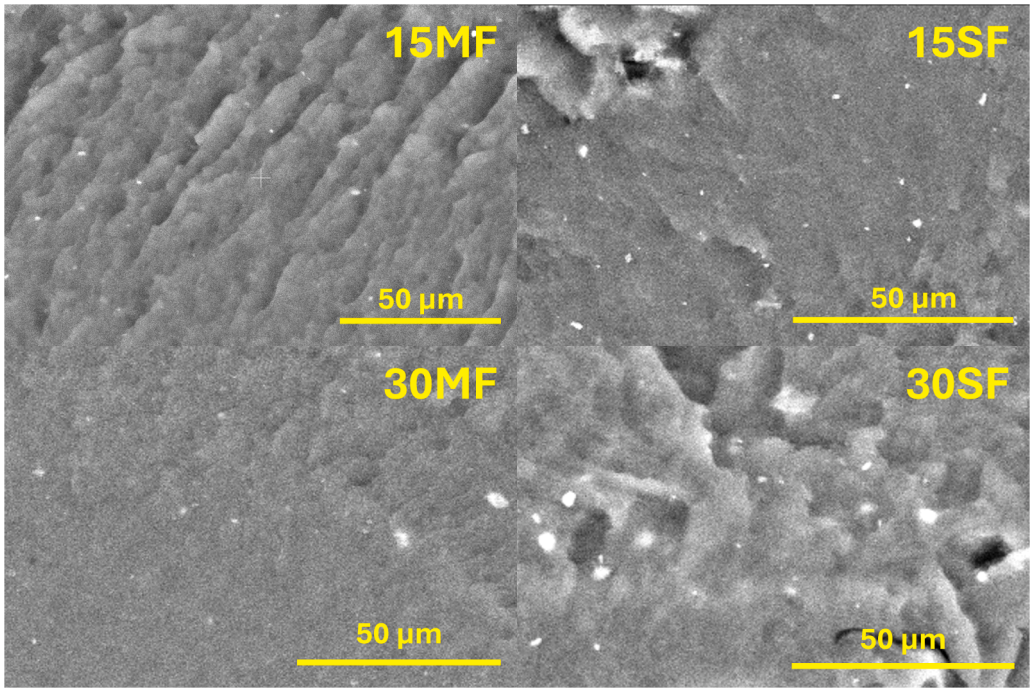

Fig. 4. SEM images of 0.50 vol% PBSA composites.

3.2. SEM of composite fracture surface

SEM images are shown in Fig. 4. SEM analysis was used to determine the dispersion of nanofiller. The polymer matrix fully covers the CNTs, and such organic filler and matrix are hard to distinguish. Therefore, in SEM, NP agglomeration distribution in the polymer matrix was looked at based on a circular backscatter detector that penetrates the composite and highlights the density difference of atoms. All composite surface fracture micrographs show filler dispersion throughout the polymer matrix. In SEM images agglomerates of ~0.5–5 μm can be seen. Additional information regarding filler distribution can be gathered indirectly from methods described in the following sections. 15MF and 15SF samples have smaller Fe_3O_4 agglomerates compared to 30MF and 30SF composite samples. SEM surface fracture micrographs indicate that composites have no visual structural defects. This observation is supported by composite density measurements summarized in supporting information (Table S3). The measured values align with theoretical rule-of-mixtures values to within ±0.6% across all compositions, indicating low void content.

3.3. 4-point sheet resistance

Fig. 5 shows the variation of sheet resistance R_s as a function of CNT volume fraction for PBSA composites. At very low filler concentrations (0.10 vol%), the composites exhibit sheet resistance $\geq 10^7$ Ω/sq indicating that the material behaves as an electrostatic dissipative material [61]. As the filler content increases, the sheet resistance decreases rapidly by several orders of magnitude. This sharp transition is identified as the percolation threshold following a percolation power law fit. The percolation threshold strongly depends on the surface modification of CNTs and dispersion quality. Among the studied systems, the pure MW and SW composites exhibit the lowest percolation threshold of 0.109 vol% and 0.098 vol% respectively, while the 15MF and 30MF composites show 0.438 vol% and 0.225 vol%, and 15SF and 30SF composites show 0.490 vol% and 0.499 vol% respectively. Above the percolation threshold the sheet resistance decreases more gradually with filler loading. In this region, a continuous three-dimensional CNT network is established throughout the PBSA matrix, allowing efficient electron transport. Consequently, further increases in filler loading produce only minor reductions in sheet resistance due to filler network densification.

3.4. Dielectric spectroscopy

Fig. 6 shows the frequency dependence of the AC electrical conductivity (σ′) for PBSA and PBSA-based composites with 0.10–2.0 vol % filler loading. The measurements were performed over a frequency range from 10^1 to 10^7 Hz. The neat polymer exhibits a typical insulator behavior, characterized by a linear increase of conductivity with frequency, which is a manifestation of the Jonscher universal dielectric response [62]. Upon the addition of conductive fillers, a 4–9 order increase in conductivity is observed across the entire frequency range. The electrical behavior of the composites can be described within three concentration regimes. Below 0.1 vol% CNT concentration, the unmodified composites exhibit strongly frequency-dependent conductivity characteristic of isolated filler clusters. In the Fe_3O_4-containing systems, however, the conductivity at equivalent CNT loadings is elevated even at the lowest concentration (0.10 vol%), indicating that Fe_3O_4 provides additional conductive pathways or bridges between otherwise disconnected CNT clusters. In the transition region (0.25–0.75 vol% for unmodified CNTs), conductivity increases by several orders of magnitude and becomes less frequency dependent, reflecting the formation and progressive densification of conductive pathways, accompanied by sharp decrease in sheet resistance. At concentration ≥ 1.0 vol%, conductivity becomes nearly frequency independent, indicating a formation of a continuous, sample-spanning network, with sheet resistance of 10^1–10^3 Ω/sq (Section 3.3). At matched volume fraction the MWCNT composites reach higher conductivity than the SWCNT composites. TUBALL SWCNTs associate into bundles through van der Waals attraction [63,64], which reduces the number of independent percolating elements per unit filler volume and places high-resistance bundle-to-bundle junctions in every conduction path. NC7000 MWCNTs disperse predominantly as individual tubes and form a denser sample-spanning network at equal volume fraction. The junction-located Fe_3O_4 agglomerates observed in the SF series (Section 3.1.4) act on precisely these bundle contacts, consistent with the higher percolation thresholds of the SF composites (Section 3.3). The incorporation of Fe_3O_4 influences network formation through competing effects. On one hand, it contributes to electrical transport, particularly in the MWCNT series, where composites (15MF, 30MF) exhibit consistently higher conductivity than their unmodified counterparts. In the SWCNT series, this effect is less systematic: 15SF shows enhanced conductivity at 0.10, 0.75, and 1.0 vol% but reduced values at 0.25–0.50 vol%, while 30SF exhibits improvement at 0.10 and 0.75 vol % with negligible change at 2.0 vol%. These reductions at intermediate loadings are consistent with sheet resistance data and likely arise from disruption of CNT dispersion by Fe_3O_4; at higher loadings (≥1.0 vol%), the CNT network dominates and Fe_3O_4 again provides a minor bridging contribution. Percolation power-law fitting of BDS conductivity at 10 Hz yielded convergence near 0.10 vol% for all series, with variations in

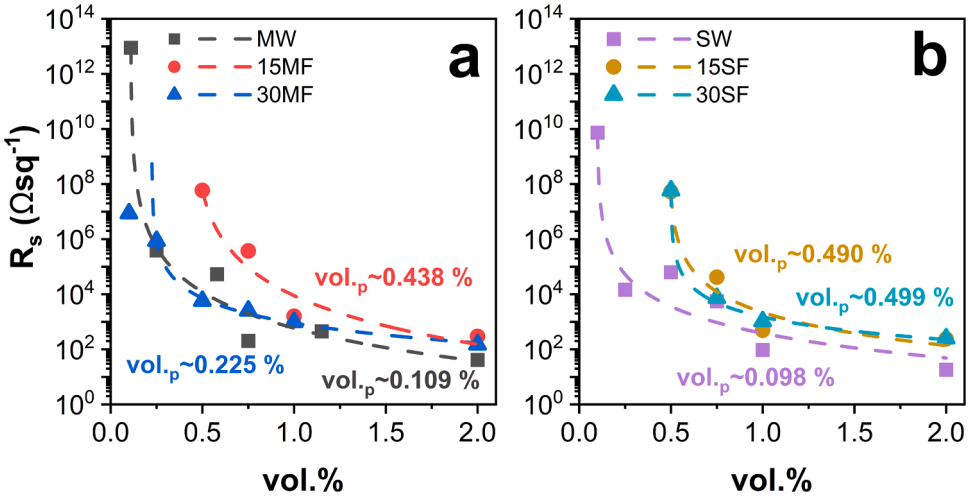

Fig. 5. Sheet resistance of (a) MW, 15MF, and 30MF and (b) SW, 15SF, and 30SF composites with power law fits of the percolation threshold.

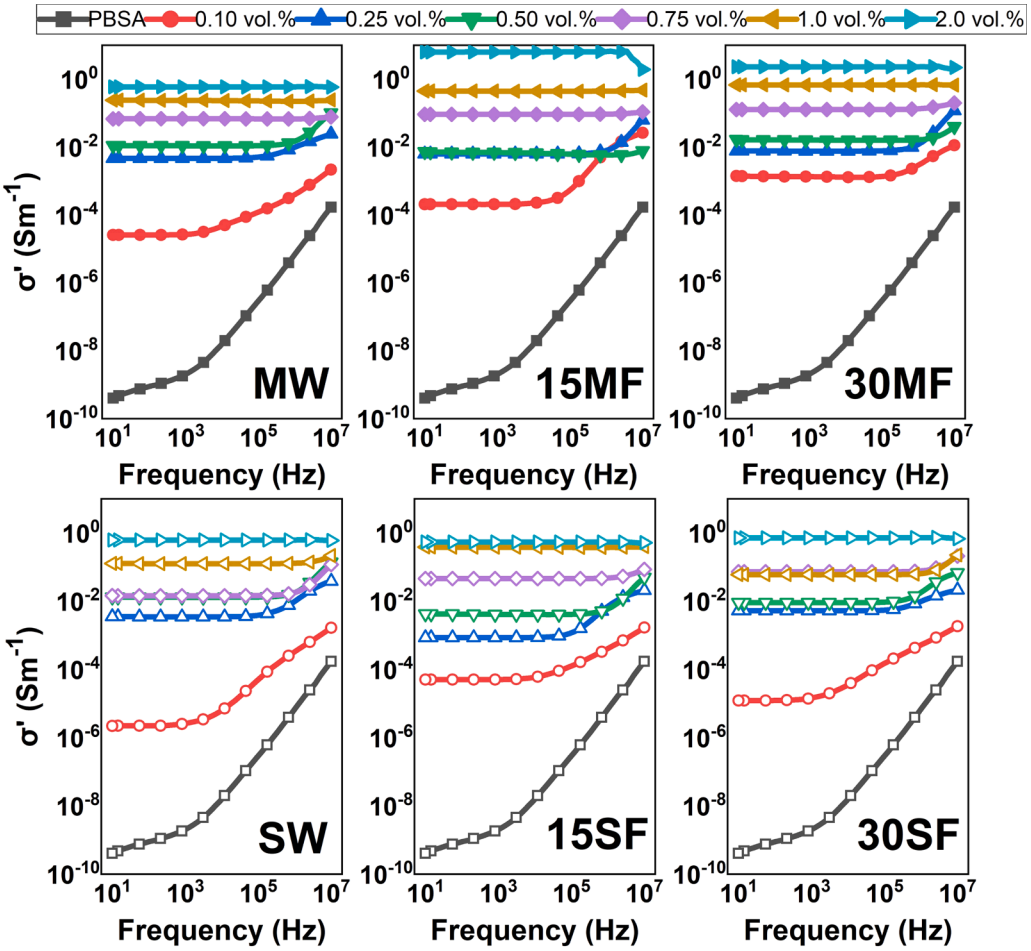

Fig. 6. AC electrical conductivity as a function of frequency for MW, 15MF, 30MF, SW, 15SF, 30SF composites and PBSA.

fitting parameters consistent with sheet resistance trends for unmodified CNTs; deviations for modified systems are attributed to filler redistribution and orientation effects induced during compression molding.

3.5. EMI SE

Reflection (R), transmission (T), and absorption (A = 1 − R − T) of 1 mm composite sheets were calculated from dielectric data across 0.1–3 GHz and 8.4–12.6 GHz for all filler loadings according to equations

$$\begin{cases} S_{11} = \dfrac{-j\left[\left(\frac{k_z}{k_{2z}}\right)^2 - 1\right]\sin(k_{2z}\tau)}{2j\left(\frac{k_z}{k_{2z}}\right)\cos(k_{2z}\tau) + \left[\left(\frac{k_z}{k_{2z}}\right)^2 + 1\right]\sin(k_{2z}\tau)} \\ S_{21} = \dfrac{2\left(\frac{k_{2z}}{k_z}\right)}{-2\left(\frac{k_{2z}}{k_z}\right)\cos(k_{2z}\tau) + j\left[\frac{k_{2z}}{k_z}^2 + 1\right]\sin(k_{2z}\tau)} \end{cases} \quad (11)$$

where S_{11} is the reflection coefficient, S_{21} is the transmission coefficient, $k_z = \frac{2\pi}{\lambda}$ and $k_{2z} = \frac{2\pi\sqrt{\varepsilon}}{\lambda}$ are wave numbers in the vacuum and the sample's media correspondingly, and τ is the thickness of the layer. The absorption (A) of the layer was calculated according to equation:

$$A = 1 - |S_{11}|^2 - |S_{21}|^2 \quad (12)$$

Unmodified MW and SW reference composites were characterized in the high band only. Full R, T, A spectra are available in supplementary Figures S4-S6. Band-averaged values are summarized in Table 3 and Fig. 7. Shielding effectiveness was decomposed as $\langle SE_T \rangle =$ –

Table 3
Band-averaged total, reflection, and absorption shielding effectiveness ($\langle SE_T \rangle$, $\langle SE_R \rangle$, $\langle SE_A \rangle$) and the $\langle SE_A \rangle$ / $\langle SE_T \rangle$ ratio for 1 mm PBSA composite sheets at 1.0 vol% and 2.0 vol% filler loading. Values are arithmetic means of $\langle SE_i \rangle(f)$ across the frequency points in each band.

Filler	vol%	$\langle SE_T \rangle$ (dB)	$\langle SE_R \rangle$ (dB)	$\langle SE_A \rangle$ (dB)	$\langle SE_A \rangle / \langle SE_T \rangle$
		Low band (0.1–3.0 GHz)			
15MF	1.0	4.6	1.4	3.2	0.70
	2.0	10.8	4.1	6.7	0.62
30MF	1.0	4.8	1.4	3.4	0.71
	2.0	8.7	3.2	5.5	0.64
15SF	1.0	1.7	0.5	1.2	0.73
	2.0	7.7	3.2	4.4	0.58
30SF	1.0	1.5	0.5	1.0	0.69
	2.0	10.1	4.2	5.9	0.59
		High band (8.4–12.6 GHz)			
MW	1.0	13.9	4.2	9.7	0.70
	2.0	11.0	3.3	7.6	0.70
15MF	1.0	14.3	4.1	10.2	0.71
	2.0	12.4	4.6	7.8	0.63
30MF	1.0	13.4	4.4	9.0	0.67
	2.0	13.8	3.8	10.0	0.73
SW	1.0	6.3	2.3	4.1	0.65
	2.0	11.7	7.6	4.1	0.35
15SF	1.0	12.5	4.4	8.1	0.65
	2.0	6.8	1.5	5.2	0.78
30SF	1.0	10.5	2.9	7.6	0.73
	2.0	6.2	3.0	3.2	0.52

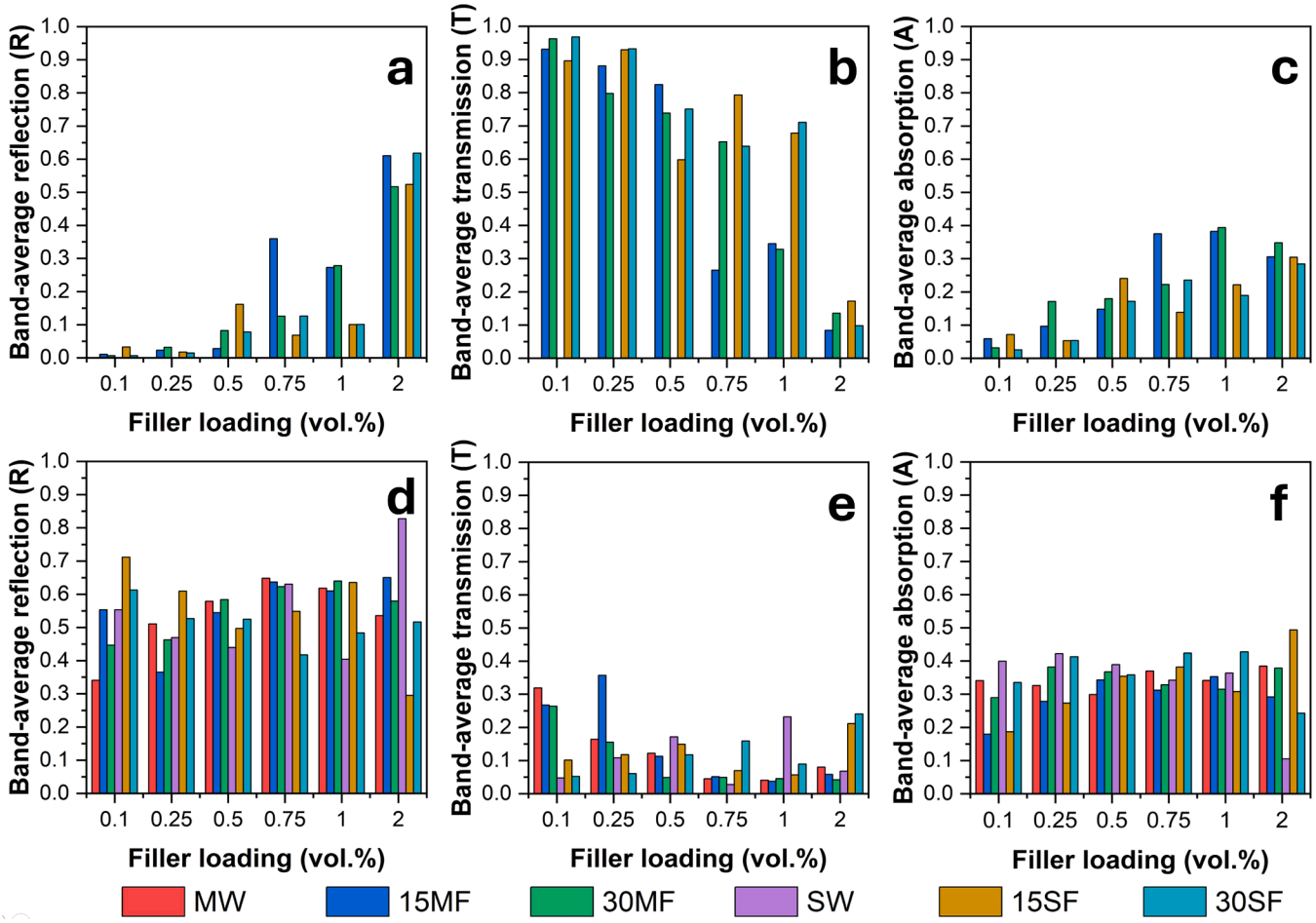

Fig. 7. Band-average reflection, transmission, and absorption of 1 mm thick nanocomposite sheets at (a-c) 0.1–3 GHz, and (d-f) 8.4–12.6 GHz frequency bands.

$10\langle \log_{10} T(f) \rangle$, $\langle SE_R \rangle = -10\langle \log_{10}(1-R(f)) \rangle$, and $\langle SE_A \rangle = \langle SE_T \rangle - \langle SE_R \rangle$, with angle brackets denoting arithmetic mean across frequency points in the band [65,66]. The dissipative share of shielding effectiveness $\langle SE_A \rangle / \langle SE_T \rangle$ is the share of the total shielding carried by dissipation rather than reflection.

For all compositions at loadings ≤ 1.0 vol%, dissipation carries more than 60% of the total shielding effectiveness in the high band ($\langle SE_A \rangle / \langle SE_T \rangle > 0.6$), while the reflected share of the incident power remains comparable to or larger than the absorbed share (Table 3, Figures S4 to S6). In the 8.4–12.6 GHz band, SW composites reach a maximum $\langle A \rangle = 0.42$ at 0.25 vol%, while MW composites remain within $\langle A \rangle = 0.30$–0.39 across the full 0.10–2.0 vol% range. SWCNT networks near percolation therefore present a composite intrinsic impedance close to η_0 at low filler content [67].

At 2.0 vol%, SW collapses: $\langle A \rangle$ falls from 0.35 to 0.11, $\langle R \rangle$ rises from ~0.41 to ~0.83, and the $\langle SE_A \rangle / \langle SE_T \rangle$ ratio drops from 0.65 to 0.35. The SF composites do not show this transition. 15SF at 2.0 vol% dissipation contributed the larger dB share with $\langle A \rangle = 0.50$, $\langle SE_T \rangle = 6.8$ dB, and $\langle SE_A \rangle / \langle SE_T \rangle$ ratio of 0.78, compared to SW's collapse to 0.35. The total SE drops relative to SW at matched loading (6.8 vs. 11.7 dB), but the dissipative share more than doubles. Fe_3O_4 agglomerates at SWCNT bundle junctions disrupt inter-bundle conductive pathways, shifting the percolation threshold from 0.098 to 0.49–0.50 vol% in the SF series (Section 3.3) and lowering the effective network conductivity at matched total loading. The SF composites at 2.0 vol% remain closer to impedance matching than SW at the same loading.

MW at 2.0 vol% retains an $\langle SE_A \rangle / \langle SE_T \rangle$ ratio of 0.70 with $\langle A \rangle = 0.40$ (Table 3, Fig. 7f); the unmodified MWCNT network does not undergo the reflection transition seen in SW. Fe_3O_4 grafting does not change the shielding regime on MWCNT and modestly raises the absorption coefficient, with 15MF and 30MF at 2.0 vol% reaching $\langle A \rangle = 0.29$ and 0.38 respectively.

In the low band at 1.0 vol% loading, both MF composites exhibit a broadband absorption plateau with $\langle A \rangle = 0.40$–0.42 and $\langle R \rangle = 0.22$ across 0.5–3 GHz. The SF composites with the same loading reach only $\langle A \rangle = 0.18$–0.22 without a plateau. At 2.0 vol% the MF plateau collapses: $\langle A \rangle$ drops to 0.31–0.34 while $\langle R \rangle$ rises to 0.52–0.61. The non-monotonic loading dependence in the MF low-band response is characteristic of impedance-matched absorption, where additional filler above the optimum contributes more to front-face reflection than to internal loss [68].

Peak reflection loss below −30 dB at quarter-wavelength thickness in the 8–18 GHz window has been reported for CNT/Fe_3O_4 composites in paraffin and rubber matrices [11,69]. Segregated network architectures in PLA and PLA/PBS blends reach total SE above 30 dB at 1–2 vol% CNT loading, with reflection carrying the majority of the shielding [15,33]. Direct reports of the reflection-absorption partition for magnetic-CNT hybrid polymer composites typically place the $\langle SE_A \rangle / \langle SE_T \rangle$ ratio at 0.55–0.70 in the 8–12 GHz band [70].

For enclosure-level shielding, a total SE near 20 dB, corresponding to 99% attenuation of the transmitted power, is a common practical target, and the values measured here, up to 13.9 dB at 1.0 vol% for a 1 mm layer, sit below it. Comparable shielding levels have been reported in the literature, although typically under substantially different material and design conditions. For example, a shielding effectiveness of 92.7 dB was achieved using a 4 mm thick petroleum-derived block copolymer containing 30 wt% hybrid filler [28], while natural rubber composites reached 63.8 dB at a thickness of 2 mm [18]. Segregated-network PLA

composites have also exceeded 30 dB with only 1–2 vol% filler [33,71]. In contrast, the present work focuses on thin, flexible, biodegradable PBSA composites prepared with substantially lower filler loadings. Although the shielding is also primarily governed by reflection, the results demonstrate that useful EMI shielding can be achieved without the high filler contents or thick sections commonly required by conventional polymer composites. Where higher shielding effectiveness is required, additional attenuation may be obtained by increasing the film thickness or by stacking multiple layers.

The 30MF composite at 2.0 vol% reaches $\langle SE_T \rangle = 13.8$ dB in the high band with $\langle SE_A/SE_T \rangle$ ratio of 0.73, and the unmodified MW at 1.0 vol% reaches $\langle SE_T \rangle = 13.9$ dB with ratio of 0.70. At 1.0 vol%, MF composites maintain $\langle A \rangle = 0.40$–0.42 across 0.5–3 GHz with $\langle SE_A/SE_T \rangle$ ratio of 0.70. These values extend dissipation contribution into a frequency window that is otherwise dominated by reflection-loss peak reports.

The low-band absorption is consistent with a dominant contribution from the dielectric response of the CNT network. Room-temperature VSM (Section 3.1.3) confirms that the deposited Fe_3O_4 and residual catalyst iron exhibit weak hysteresis with low coercivity and remanence. However, VSM does not provide frequency-dependent complex permeability and therefore cannot quantify or exclude magnetic relaxation or resonance losses in the investigated bands. Nevertheless, the MF plateau and its absence in the SF composites correlate with the conductive-network differences described above, specifically the lower MF percolation threshold and the junction-localized SF agglomerates. Conductive-network modification is therefore considered the interpretation most consistent with the available data, although a magnetic-loss contribution cannot be entirely excluded.

3.6. Crystallization and thermal conductivity

Representative DSC thermograms from the cooling and second heating cycles at 0.50 vol% filler loading are shown in Figs. 8a and 8b; the extracted parameters are summarized in Table 4. Table 4 includes the crystallization temperature (T_c), melting enthalpy (ΔH_m), degree of crystallinity (χ_c), and melting temperature (T_m). Neat PBSA crystallizes at 30.8 °C with a degree of crystallinity of 34%. All filler additions shift the crystallization exotherm upward by 26–30 °C, with SW showing the

Table 4
DSC thermal properties of 0.50 vol% PBSA composites.

Sample	Cooling	1st heating		2nd heating		
	T_c (°C)	ΔH_m (J·g^{-1})	χ_c (%)	T_m (°C)	ΔH_m (J·g^{-1})	χ_c (%)
PBSA	30.8	45.8	42%	87.6	37.9	34%
MW	57.4	49.1	45%	89.3	50.7	46%
15MF	59.3	40.6	38%	88.8	49.2	45%
30MF	60.9	48.1	44%	88.8	45.2	41%
SW	61.2	44.3	40%	88.6	54.3	50%
15SF	60.6	48.2	44%	88.3	49.6	45%
30SF	59.5	50.0	46%	88.5	53.8	49%

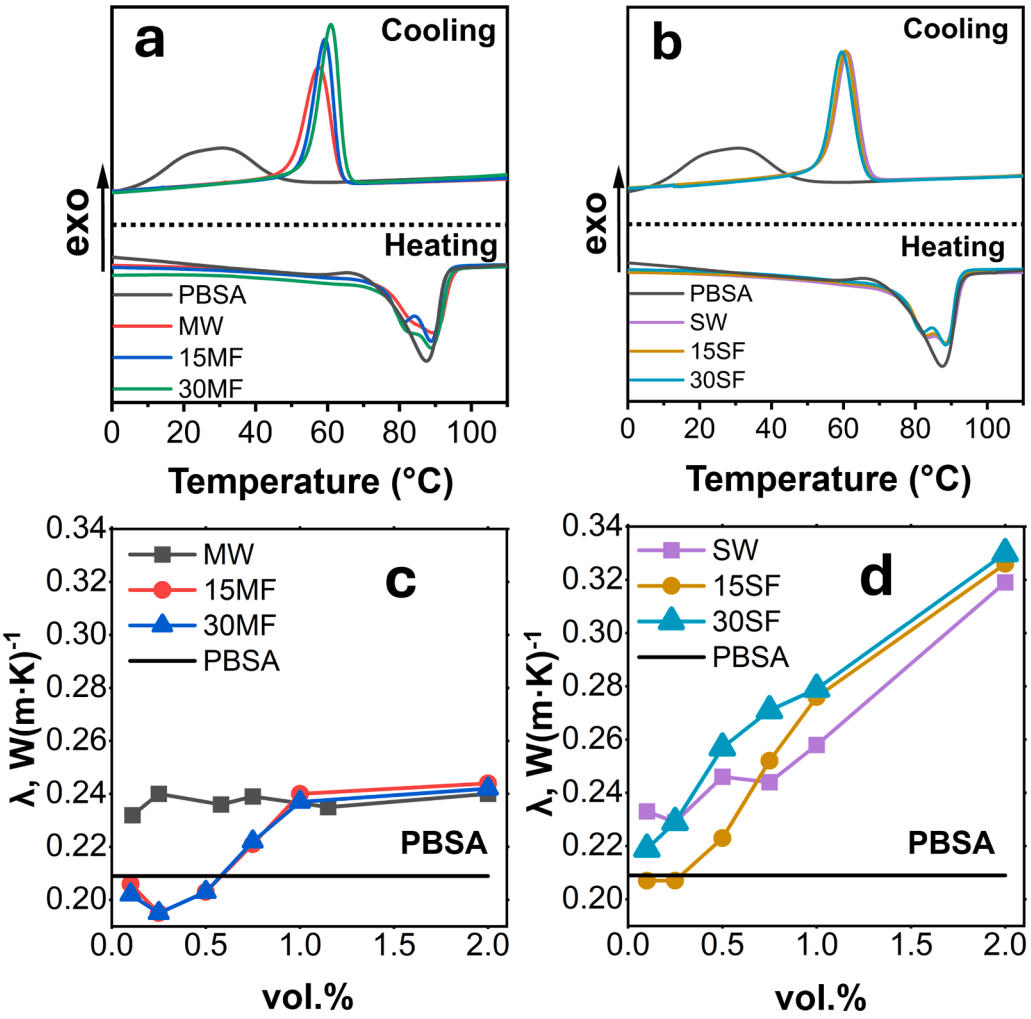

Fig. 8. DSC curves of cooling and second heating for (a) MW, 15MF, 30MF and (b) SW, 15SF, 30SF 0.50 vol% composites; Thermal conductivity of (c) MW, 15MF, 30MF and (d) SW, 15SF, 30SF composites;.

highest T_c (61.2 °C) and MW the lowest among the filled samples (57.4 °C). This shift reflects efficient heterogeneous nucleation of PBSA on the CNT surface, consistent with the nucleating behavior of CNTs reported in other polyester systems [72–75].

The degree of crystallinity increases to 41–50% across the filled compositions. The unmodified CNT composites produce the highest values (SW 50%, MW 46%), while the Fe_3O_4-grafted systems are lower (15MF 45%, 30MF 41%, 15SF 45%, 30SF 49%). Higher content of grafted Fe_3O_4 correlates with lower composite crystallinity. This can be attributed to the partial coverage of the CNT surface by nanoparticles, which reduces nucleation efficiency by limiting the accessible surface area [76,77].

The composite second heating curves exhibit a secondary endotherm at 84–86 °C that is absent in neat PBSA. This double melting is attributed to the melting of thinner lamellae formed during CNT-induced heterogeneous nucleation [36]. No cold crystallization exotherm was observed during heating, consistent with near-complete crystallization during cooling.

Figs. 8c and 8d shows the thermal conductivity of the composites at 25 °C against total filler volume fraction. The numerical thermal conductivity values are shown in Table S7. Neat PBSA measured 0.209 $Wm^{-1}K^{-1}$. The dependence of thermal conductivity on filler concentration differs markedly between two CNT types. The MW composites show a flat response: thermal conductivity varies between 0.232 and 0.240 $Wm^{-1}K^{-1}$ across the entire 0.10–2.0 vol% range, corresponding to a total variation of 0.008 $Wm^{-1}K^{-1}$ over a 20-fold change in filler concentration. In the SW composites thermal conductivity increases steadily with filler loading: 0.233 $Wm^{-1}K^{-1}$ at 0.10 vol% to 0.319 $Wm^{-1}K^{-1}$ at 2.0 vol% (an improvement of 53%), with no plateau.

DSC shows that 0.50 vol% CNT increases PBSA crystallinity from 34 to 41–50% (Table 4, 2nd heating), and crystalline domains in semi-crystalline polymers conduct phonons more efficiently than the amorphous phase due to ordered chain packing [78–80]. However, the overall changes in crystallinity can be considered relatively small, indicating that variations in thermal conductivity are likely governed by other mechanisms.

The gradual rise in the SW series could be attributed to phonon transport through an extended SWCNT bundle network. SWCNTs aggregate into bundles via van der Waals interactions [63,64], forming thermal pathways with effective aspect ratios exceeding those of individual MWCNTs. The intrinsic thermal conductivity of individual SWCNTs (~3500 $Wm^{-1}K^{-1}$) substantially exceeds that of MWCNTs (~2000 $Wm^{-1}K^{-1}$) [81–83], while bundling introduces additional intertube thermal resistance that reduces the effective conductivity of the bundle network [64]. At 2.0 vol% the SW curve is still rising, indicating that bundle network formation has not saturated. An alternative explanation is that the MWCNT network contribution saturates at low loading, because inter-tube contact resistance caps the effective network thermal conductivity [84,85].

The Fe_3O_4 grafting produces divergent effects on the two CNT types. 15MF and 30MF overlap across the full concentration range and approach the MW values only above 1.0 vol%. Below 0.50 vol%, both MF composites show thermal conductivities at or below that of neat PBSA, reaching 0.195 $Wm^{-1}K^{-1}$ at 0.25 vol% ($\Delta\lambda = -0.014$ $Wm^{-1}K^{-1}$ relative to neat PBSA). The depression appears in both 15MF and 30MF systematically. The introduction of additional filler-matrix and filler-CNT interfaces also increases the interfacial thermal resistance [86,87], which at low filler concentrations may dominate over the conductive contribution of the oxide phase.

In the SF composites, 30SF consistently exceeds 15SF at all loadings below 1.0 vol% (0.219 vs. 0.207 $Wm^{-1}K^{-1}$ at 0.10 vol%; 0.257 vs. 0.223 $Wm^{-1}K^{-1}$ at 0.50 vol%), the opposite ordering to what would be expected from additional interfacial phonon scattering. At 2.0 vol%, both 15SF and 30SF exceed SW (0.326 and 0.330 vs. 0.319 $Wm^{-1}K^{-1}$) despite containing approximately 1.90 and 1.81 vol% SWCNT, respectively, after subtracting the Fe_3O_4 fraction. STEM shows that Fe_3O_4 in the SF systems form large agglomerates concentrated at the junctions between SWCNT bundles (Fig. 3, 15SF and 30SF). If inter-bundle contact resistance limits thermal transport in SWCNT networks [88,89], Fe_3O_4 clusters positioned at these junctions could reduce the effective junction resistance by providing additional phonon transport pathways through the crystalline oxide phase. The 30SF > 15SF ordering at low loadings is consistent with this, since 30SF presents larger and more numerous agglomerates per unit SWCNT length. The convergence of 15SF and 30SF at 2.0 vol% (~ 0.33 $Wm^{-1}K^{-1}$) could reflect saturation of bridgeable junction sites. Confirming this mechanism would require direct measurement of the junction thermal conductance, for example by comparing composites prepared from pre-bundled versus individually dispersed SWCNTs.

3.7. Thermal stability and rheological properties

Thermogravimetric analysis in air is shown in Figs. 9a and 9b. The DTG is shown in Figure S8. Table 5 summarizes the temperatures at which 5% (T_5) and 50% (T_{50}) mass loss occur, as well as the maximum degradation temperature (T_{max}). Neat PBSA degrades with $T_5 = 356$ °C, $T_{50} = 396$ °C, and $T_{max} = 399$ °C. The unmodified 0.50 vol% CNT composites retain comparable stability (MW $T_5 = 351$ °C; SW $T_5 = 337$ °C), with T_{50} and T_{max} within a few degrees of the neat polymer.

The Fe_3O_4-grafted systems show onset reductions that depend on both Fe_3O_4 content and CNT type. In the MWCNT series, T_5 decreases from 351 °C (MW) to 339 °C (15MF) to 322 °C (30MF), a 29 °C reduction at 30 wt% Fe_3O_4. In the SWCNT series, T_5 instead increases slightly from 337 °C (SW) to 343 °C (15SF) and 344 °C (30SF). T_{50} and T_{max} follow the same trends, with 30MF showing the lowest values (383 °C and 393 °C, respectively).

Metal oxide nanofillers are known to catalytically accelerate the thermo-oxidative degradation of polyester matrices through radical-mediated pathways [90,91] and this catalytic activity scales with the accessible filler surface area rather than total mass [92]. All compositions retain adequate stability for processing at the compression molding temperature of 135 °C. The Fe_3O_4-induced destabilization is therefore not relevant for short-term melt processing at 135 °C.

Complex viscosity (η*) at 140 °C was measured across 0.1–100 rad s^{-1} on neat PBSA and the 0.50 vol% composites (Fig. 9c, d). Neat PBSA exhibited an approximate Newtonian plateau in η* below ~10 rad s^{-1} . All composites at 0.50 vol% showed power-law shear thinning across the full frequency range with no Newtonian plateau, and η* at 1 rad s^{-1} was approximately one order of magnitude above neat PBSA. The loss of the terminal viscous plateau in η* is a signature of a percolated filler network that constrains polymer chain relaxation in the melt [93,94]. The rheological percolation in the melt is consistent with the electrical percolation in the solid state (Section 3.3), although the two thresholds need not coincide. The Fe_3O_4-grafted CNTs containing composites showed lower η* than the unmodified CNT composites at matched total loading, reflecting the reduced effective CNT volume fraction in the hybrid fillers.

3.8. Thermomechanical and mechanical behavior

Dynamic mechanical analysis at 0.50 vol% filler loading is shown in Fig. 10a-d and Table 6. Neat PBSA exhibited a storage modulus (E′) of 298 MPa at 20 °C and a tan δ peak at −32 °C, corresponding to the glass transition temperature (T_g). The addition of MWCNTs shifted T_g to higher temperatures (up to −28 °C), indicating restricted polymer chain mobility and the presence of interfacial interactions between CNTs and the PBSA matrix [29,95]. This behavior may be associated with the formation of a percolated filler network. If an effective reinforcing network is present, a sustained increase in storage modulus in the viscoelastic region is expected [29,95]. Such an enhancement is

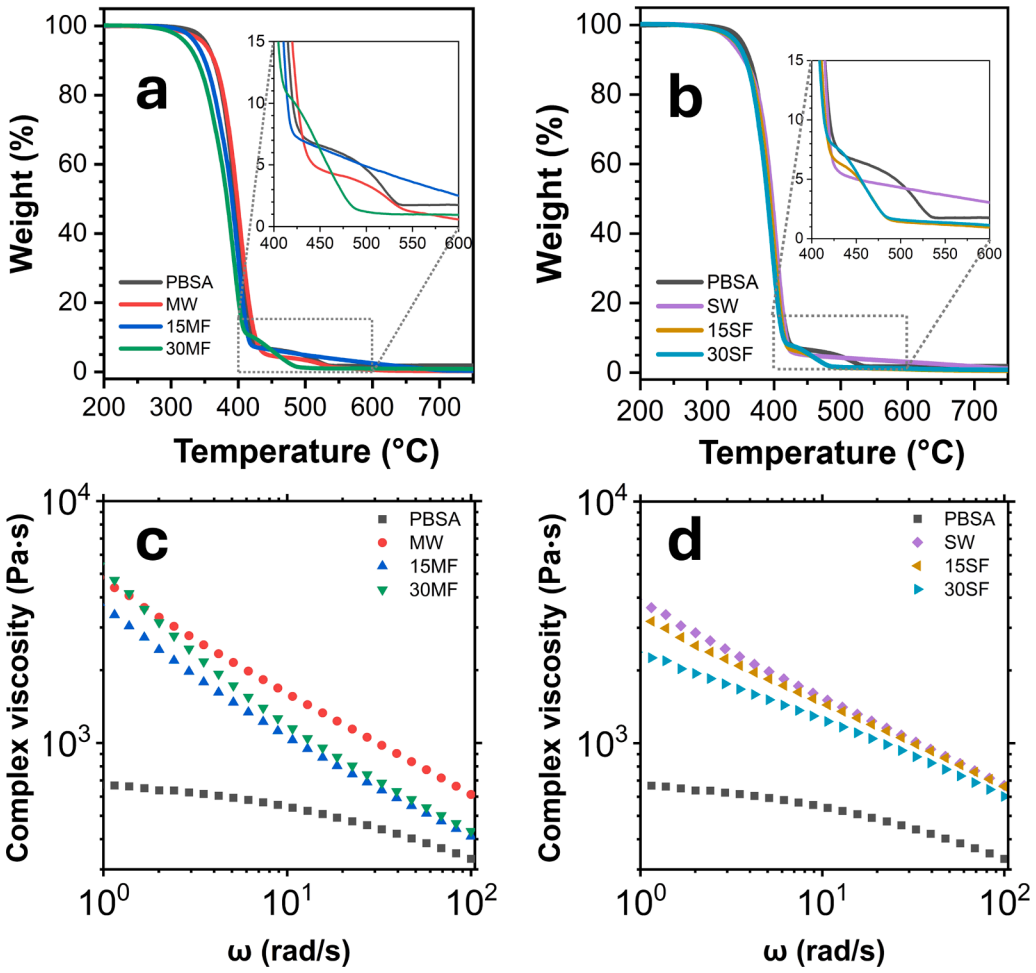

Fig. 9. TGA curves of (a) MW, 15MF, 30MF and (b) SW, 15SF, 30SF 0.50 vol% composites; (c, d) Complex viscosity η* at 140 °C as a function of angular frequency for the 0.50 vol% composites in the MWCNT and SWCNT families, respectively, with neat PBSA shown for comparison.

Table 5
Thermal stability of 0.50 vol% PBSA composites.

Sample	T_5 (°C)	T_{50} (°C)	T_{max} (°C)
PBSA	356	396	399
MW	351	398	403
15MF	339	391	399
30MF	322	383	393
SW	337	397	402
15SF	343	394	400
30SF	344	390	397

observed for both MWCNT and SWCNT-filled systems. Notably, SWCNTs provide a more pronounced increase in E′, which can be attributed to their higher aspect ratio and greater ability to form interconnected networks.

In the case of SWCNT composites, a decrease in E′ with increasing Fe_3O_4 nanoparticle content suggests that CNTs are primarily responsible for mechanical reinforcement. In contrast, MWCNT-filled composites exhibit a lower overall enhancement in E′, indicating that percolated network is not formed to the same extent as in SWCNT systems. Consequently, the differences between grafted and non-grafted MWCNTs remain within experimental error.

Above T_g the matrix contribution to stiffness has reduced and the storage modulus reflects the filler network directly. At 20 °C the E′ of the SWCNT composites exceeds neat PBSA by 37–78%, compared with 3–26% at −60 °C in the glassy region, and the relative reinforcement is larger in the rubbery region than in the glassy region, which identifies the percolated filler network rather than glassy-state stiffening as the origin of the enhancement [29,95].

Elastic modulus (E) and ultimate tensile strength (σ) are compared between composite loadings at Figs. 10e and 10f and values with error values are summarized in Table 7. Neat PBSA has E of 249 MPa and σ of 16.3 MPa. Elastic modulus rose with filler loading in all six composition series (Fig. 10e). Composites with SWCNT had higher E values compared to ones with MWCNT in almost all tested concentrations. The SWCNT/MWCNT comparison aligns with the aspect-ratio difference between the two CNT types [96]. At 2.0 vol% loading the highest modulus values were achieved by 15SF 546 MPa and 15MF 333 MPa. Within each CNT series the 15 wt% Fe_3O_4 variant exceeded both the unmodified CNT and the 30 wt% variant at matched total loading (15MF > MW > 30MF; 15SF > SW > 30SF), and this ordering was preserved at 1.0, 0.50, and 0.25 vol%.

Ultimate strength rose from 16.3 MPa to 23.0–23.1 MPa for SW and 15SF at 2.0 vol%, a 42% increase (Fig. 10f). Most compositions saturated above 0.50 vol% in the 18–20 MPa range; SW and 15SF continued to rise beyond 1.0 vol%. The relative increase in tensile strength is smaller than that observed for the modulus (120% for 15SF at 2.0 vol%), indicating that load transfer through the CNT network is more effective in the elastic regime, while deformation in the plastic regime remains largely governed by the matrix. As the 15 wt% Fe_3O_4 variants exhibited the highest modulus and strength, this suggests a possible synergistic effect, where a moderate amount of grafted Fe_3O_4 reduces CNT agglomeration.

Representative stress-strain curves of 1.0 vol% composites are shown

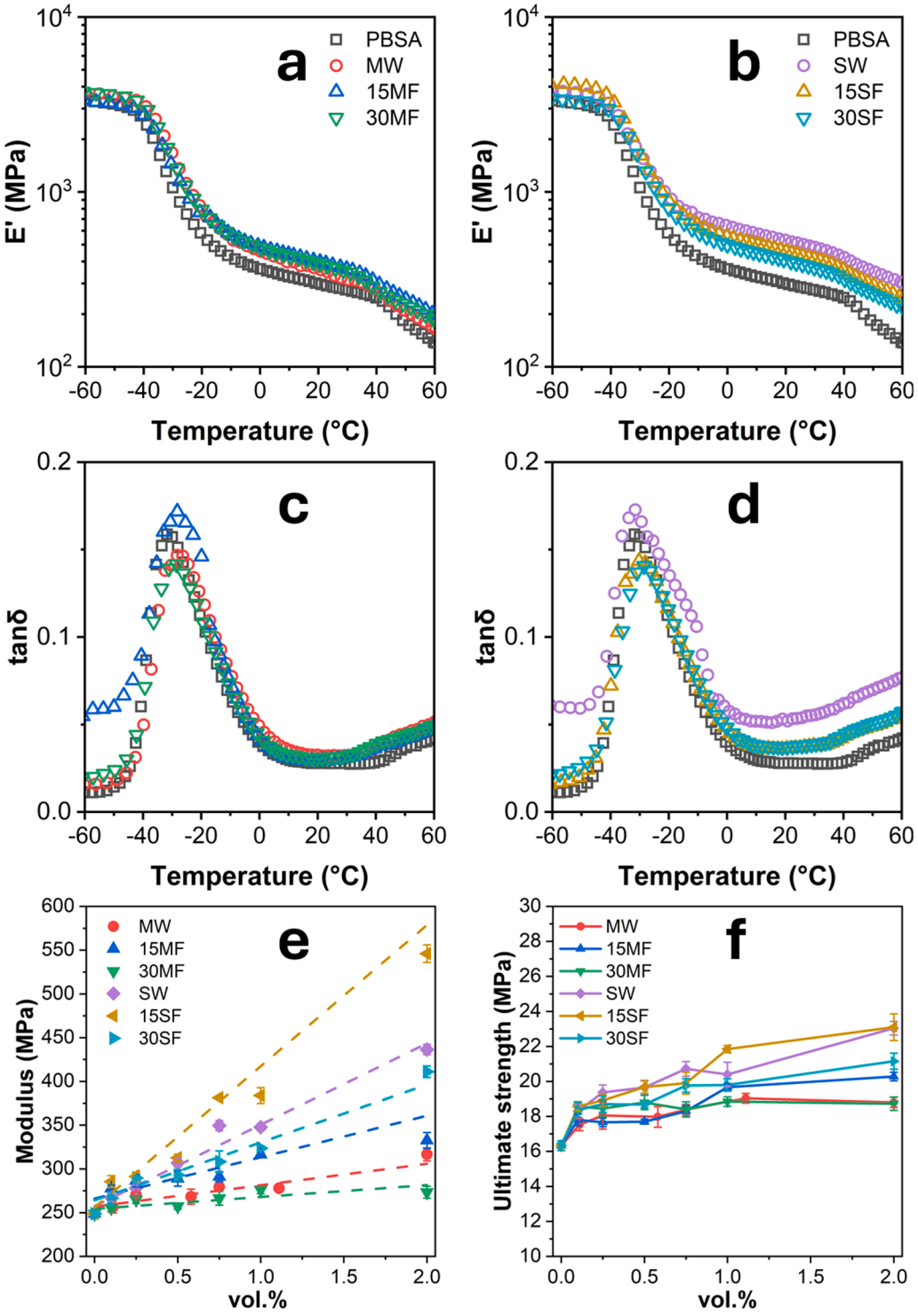

Fig. 10. Thermomechanical and mechanical properties of PBSA composites. (a, b) Storage modulus E′ and (c, d) tan δ from dynamic mechanical analysis on the 0.50 vol% composites, measured at 1 Hz from −60–60 °C for MWCNT and SWCNT families, respectively with neat PBSA shown for comparison. (e) Elastic modulus and (f) ultimate strength as a function of filler volume fraction for all six composition series (MW, 15MF, 30MF, SW, 15SF, 30SF). Dashed lines in (e) are linear guides to the eye. Error bars in (e, f) represent one standard deviation across five tensile specimens.

in supplementary Figure S9. PBSA exhibited soft and ductile behavior with pronounced serrated plastic flow. The serrated plastic flow led to relatively large variations in elongation at break values (146–301%). Similar observations have been reported in the literature [97]. The incorporation of SWCNT fillers suppresses this serrated flow behavior. The addition of CNTs led to the reduction of elongation at break values, which can be attributed to restricted polymer chain mobility.

4. Conclusion

In this work, multi- and single-walled carbon nanotubes were successfully grafted with Fe_3O_4 via aqueous co-precipitation without prior functionalization, forming well-defined hybrid structures as confirmed by XRD and STEM. The deposited Fe_3O_4 crystallite sizes were ~3–8 nm (XRD), and ~10 nm (STEM) was present on CNT surfaces as both

Table 6
DMA properties of PBSA composites, with neat PBSA shown for comparison.

Sample	E' (MPa)			T_g (°C)
	−60 °C	20 °C	60 °C	
PBSA	3327	298	137	−31.3
MW	3694	363	167	−27.3
15MF	3345	398	198	−28.2
30MF	3724	388	187	−29.2
SW	3841	529	301	−31.5
15SF	4205	457	242	−28.6
30SF	3417	408	216	−28.5

Table 7
Tensile properties of neat PBSA and its composites.

Filler	vol%	Elastic modulus (MPa)	Ultimate strength (MPa)
PBSA	-	248.7 ± 4.5	16.3 ± 0.3
MW	0.10	256.3 ± 6.7	17.5 ± 0.3
	0.25	270.6 ± 3.2	18.1 ± 0.8
	0.58	268.3 ± 8.7	18.0 ± 0.6
	0.75	279.4 ± 4.9	18.4 ± 0.3
	1.15	278.0 ± 3.2	19.0 ± 0.3
	2.0	316.6 ± 7.6	18.8 ± 0.3
15MF	0.10	277.7 ± 3.7	17.8 ± 0.3
	0.25	286.5 ± 7.1	17.7 ± 0.2
	0.50	289.2 ± 8.8	17.7 ± 0.1
	0.75	291.1 ± 5.7	18.3 ± 0.3
	1.0	316.4 ± 1.9	19.7 ± 0.2
	2.0	332.6 ± 9.1	20.3 ± 0.2
30MF	0.10	255.4 ± 4.4	18.6 ± 0.3
	0.25	264.9 ± 4.4	18.5 ± 0.5
	0.50	257.3 ± 3.4	18.8 ± 0.4
	0.75	266.4 ± 7.8	18.4 ± 0.4
	1.0	276.3 ± 4.6	18.9 ± 0.3
	2.0	273.3 ± 6.8	18.7 ± 0.4
SW	0.10	267.2 ± 4.6	18.3 ± 0.4
	0.25	278.0 ± 8.6	19.4 ± 0.4
	0.50	306.9 ± 4.6	19.7 ± 0.4
	0.75	349.5 ± 5.8	20.7 ± 0.4
	1.0	347.8 ± 4.0	20.4 ± 0.7
	2.0	436.4 ± 6.0	23.0 ± 0.4
15SF	0.10	285.5 ± 6.8	18.6 ± 0.3
	0.25	291.2 ± 5.0	18.9 ± 0.4
	0.50	312.6 ± 4.3	19.7 ± 0.3
	0.75	381.4 ± 1.4	19.9 ± 0.6
	1.0	383.8 ± 9.0	21.9 ± 0.2
	2.0	546.0 ± 10.1	23.1 ± 0.8
30SF	0.10	266.3 ± 7.5	18.4 ± 0.4
	0.25	289.6 ± 2.3	18.7 ± 0.5
	0.50	293.0 ± 6.3	18.7 ± 0.2
	0.75	308.3 ± 12.3	19.8 ± 0.4
	1.0	323.6 ± 2.5	19.8 ± 0.4
	2.0	411.1 ± 6.5	21.2 ± 0.5

individual particles and agglomerates (~50–550 nm, STEM). Magnetometry showed that the deposited Fe_3O_4 was superparamagnetic, with a specific magnetization calculated to range from 4.7 to 65 emu/g, depending on crystallite size.

The incorporation of CNTs led to the formation of conductive networks, achieving volume conductivity up to 6.3 S m^{-1} at 2.0 vol% loading, corresponding to an increase of approximately 10 orders of magnitude compared to neat PBSA. Sheet resistance was reduced by up to six orders of magnitude, achieving effective surface percolation at approximately 0.1–0.5 vol% filler loading. Dissipation carried the majority of the total shielding effectiveness in most compositions, with $\langle SE_A \rangle$ / $\langle SE_T \rangle$ ratios of 0.58–0.73 in the 0.1–3 GHz band and up to 0.78 in the 8.4–12.6 GHz band. By the incident power balance, absorption exceeded reflection for the Fe_3O_4-grafted MWCNT composites at 1.0 vol % below 3 GHz and for 15SF at 2.0 vol% at 8.4–12.6 GHz, whereas unmodified SWCNT at 2.0 vol% transitioned to reflection-dominated shielding.

Tensile properties showed increases of up to 120% in elastic modulus and 42% in tensile strength, while dynamic mechanical analysis confirmed the formation of a reinforcing network in the viscoelastic state and thermal conductivity improved by up to 58%. Mechanical and thermal property enhancements increased with filler loading and were more pronounced for SWCNT-based systems. These results identify CNT wall structure and Fe_3O_4 distribution as design variables for the reflection/absorption partition of thin shielding films at filler contents of 2.0 vol% and below.

CRediT authorship contribution statement

Krisjanis Smits: Methodology, Investigation. **Mikhail Maiorov:** Investigation, Methodology. **Oskars Platnieks:** Writing – review & editing, Methodology, Formal analysis. **Dzmitry Tsyhanok:** Methodology, Investigation. **Juras Banys:** Writing – review & editing. **Jan Macutkevič:** Writing – review & editing, Methodology, Investigation. **Artis Krikovs:** Writing – original draft, Visualization, Validation, Investigation, Formal analysis. **Miks Bleija:** Writing – original draft, Validation, Methodology, Investigation, Formal analysis, Conceptualization. **Sergejs Gaidukovs:** Writing – review & editing, Supervision, Resources, Project administration, Methodology, Funding acquisition, Conceptualization.

Declaration of Competing Interest

The authors declare that they have no known competing financial interests or personal relationships that could have appeared to influence the work reported in this paper.

Acknowledgments

This work was supported by the Project No: OSI_PIP_BioPhoT−2025/1–0073: “Resilient Shielding for High-Integrity EMI Protected Cybersecurity Applications” implemented under the long-term national research programme "Innovation Fund— Long-Term Research Programme" project “IVPP-EM-Innovation−2024/1–0002 "Biomedical and Photonics Research Platform for Innovative Products (BioPhoT)". Work at Vilnius University was supported by Campus France and the Lithuanian Science Council through the joint program PHC Gilibert #52146XD “3D-printed structures for electromagnetic applications”. A.K. acknowledges support from Riga Technical University through the master’s student grant project “Nr. ZM−2026/5” for strengthening scientific personnel capacity in 2025/2026.

Appendix A. Supporting information

Supplementary data associated with this article can be found in the online version at doi:10.1016/j.synthmet.2026.118263.

Data availability

Data will be made available on request.

References

[1] M. SH, P. Joseph, S. George, Electromagnetic interference shielding: a comprehensive review of materials, mechanisms, and applications, Nanoscale Adv. 7 (15) (Jul 22 2025) 4510–4534, https://doi.org/10.1039/d5na00240k.
[2] M. Bleija, O. Platnieks, J. Macutkevič, et al., Poly(Butylene Succinate) hybrid multi-walled carbon nanotube/iron oxide nanocomposites: electromagnetic shielding and thermal properties, Polymers 15 (3) (2023), https://doi.org/10.3390/polym15030515.
[3] F. Shahzad, M. Alhabeb, C.B. Hatter, et al., Electromagnetic interference shielding with 2D transition metal carbides (MXenes), Science 353 (6304) (Sep 9 2016) 1137–1140, https://doi.org/10.1126/science.aag2421.
[4] K. Zeranska, K. Filak, K. Wilczyński, et al., Graphene-based thermoplastic composites as extremely broadband and frequency-dependent EMI absorbers for

multifunctional applications, Acs Appl. Electron. Ma. 4 (9) (2022) 4463–4470, https://doi.org/10.1021/acsaelm.2c00722.
[5] N. Chikyu, T. Nakano, G. Kletetschka, Y. Inoue, Excellent electromagnetic interference shielding characteristics of a unidirectionally oriented thin multiwalled carbon nanotube/polyethylene film, Mater. & Des. (2020) 195, https://doi.org/10.1016/j.matdes.2020.108918.
[6] S. Geetha, K.K. Satheesh Kumar, C.R.K. Rao, M. Vijayan, D.C. Trivedi, EMI shielding: methods and materials—a review, J. Appl. Polym. Sci. 112 (4) (May 15 2009) 2073–2086, https://doi.org/10.1002/app.29812.
[7] W. Barmore, H. Patel, C. Voong, C. Tarallo, J.B. Calkins Jr., Effects of medically generated electromagnetic interference from medical devices on cardiac implantable electronic devices: a review, World J. Cardiol. 14 (8) (Aug 26 2022) 446–453, https://doi.org/10.4330/wjc.v14.i8.446.
[8] Q.-D. Nguyen, C.-G. Choi, Recent advances in multifunctional electromagnetic interference shielding materials, Heliyon 10 (10) (2024), https://doi.org/10.1016/j.heliyon.2024.e31118.
[9] K. Shahapurkar, M. Gelaw, V. Tirth, et al., Comprehensive review on polymer composites as electromagnetic interference shielding materials, Polym. Polym. Compos. (2022) 30, https://doi.org/10.1177/09673911221102127.
[10] R.K. Bheema, J.G. Bhaskaran, K. Verma, A. Chavali, M. Etika, A review on recent progress in polymer composites for effective electromagnetic interference shielding properties - structures, process, and sustainability approaches, Nanoscale Adv. 6 (23) (Sep 26 2024) 5773–5802, https://doi.org/10.1039/D4NA00572D.
[11] M.S. Saeed, J. Seyed-Yazdi, S.H. Hekmatara, Surface modification of MWCNT with cluster form of Fe2O3/Fe3O4 NPs for improving their microwave absorption performance, Chem. Phys. Lett. (2020) 756, https://doi.org/10.1016/j.cplett.2020.137823.
[12] Y. Kato, M. Horibe, S. Ata, T. Yamada, K. Hata, Stretchable electromagnetic-interference shielding materials made of a long single-walled carbon-nanotube–elastomer composite, RSC Adv. 7 (18) (2017) 10841–10847, https://doi.org/10.1039/C6RA25350D.
[13] Z. Liu, G. Bai, Y. Huang, et al., Reflection and absorption contributions to the electromagnetic interference shielding of single-walled carbon nanotube/polyurethane composites, Carbon 45 (4) (2007) 821–827, https://doi.org/10.1016/j.carbon.2006.11.020.
[14] P. Verma, P. Saini, R.S. Malik, V. Choudhary, Excellent electromagnetic interference shielding and mechanical properties of high loading carbon-nanotubes/polymer composites designed using melt recirculation equipped twin-screw extruder, Carbon 89 (2015) 308–317, https://doi.org/10.1016/j.carbon.2015.03.063.
[15] G.D. Tian, H.Z. He, M.H. Xu, Y.F. Liu, Q. Gao, Z.W. Zhu, Ultralow percolation threshold biodegradable PLA/PBS/MWCNTs with segregated conductive networks for high-performance electromagnetic interference shielding applications, J. Appl. Polym. Sci. 140 (9) (Mar 5 2023), https://doi.org/10.1002/app.53558.
[16] S. Rathinavel, K. Priyadharshini, D. Panda, A review on carbon nanotube: An overview of synthesis, properties, functionalization, characterization, and the application, Mater. Sci. Eng. B-Adv. (2021) 268, https://doi.org/10.1016/j.mseb.2021.115095.
[17] W. Yang, B. Jiang, S. Che, L. Yan, Z.-x Li, Y.-f Li, Research progress on carbon-based materials for electromagnetic wave absorption and the related mechanisms, New. Carbon Mater. 36 (6) (2021) 1016–1030, https://doi.org/10.1016/S1872-5805(21)60095-1.
[18] Z. Wei, Y. Cai, Y. Zhan, et al., Ultra-Low Loading of Ultra-Small Fe(3) O(4) Nanoparticles on Nonmodified CNTs to Improve Green EMI Shielding Capability of Rubber Composites, Small 20 (9) (Mar 2024) e2307148, https://doi.org/10.1002/smll.202307148.
[19] N. Li, G.W. Huang, Y.Q. Li, et al., Enhanced Microwave Absorption Performance of Coated Carbon Nanotubes by Optimizing the Fe(3)O(4) Nanocoating Structure, ACS Appl. Mater. Interfaces 9 (3) (Jan 25 2017) 2973–2983, https://doi.org/10.1021/acsami.6b13142.
[20] J. Yang, X. Liao, J. Li, et al., Light-weight and flexible silicone rubber/MWCNTs/Fe3O4 nanocomposite foams for efficient electromagnetic interference shielding and microwave absorption, Compos. Sci. Technol. (2019) 181, https://doi.org/10.1016/j.compscitech.2019.05.027.
[21] D.M. Pozar. Microwave Engineering, 4th ed. ed., Wiley-IEEE Press, 2012.
[22] C. Wu, J. Wang, X. Zhang, et al., Hollow gradient-structured iron-anchored carbon nanospheres for enhanced electromagnetic wave absorption, Nano-Micro Lett. 15 (1) (Dec 2023) 7, https://doi.org/10.1007/s40820-022-00963-w.
[23] Y.Q. Wang, R. Ding, Y.C. Zhang, et al., Gradient Hierarchical Hollow Heterostructures of Ti(3)C(2)T(x)@rGO@MoS(2) for Efficient Microwave Absorption, ACS Appl. Mater. Interfaces 15 (27) (Jul 12 2023) 32803–32813, https://doi.org/10.1021/acsami.3c06860.
[24] R. Yu, C.-F. Jiang, W. Chu, M.-F. Ran, W.-J. Sun, Decoration of CNTs' surface by Fe3O4 nanoparticles: influence of ultrasonication time on the magnetic and structural properties, Chin. Chem. Lett. 28 (2) (2017) 302–306, https://doi.org/10.1016/j.cclet.2016.07.014.
[25] X. Wang, Z. Zhao, J. Qu, Z. Wang, J. Qiu, Fabrication and characterization of magnetic Fe3O4–CNT composites, J. Phys. Chem. Solids 71 (4) (2010) 673–676, https://doi.org/10.1016/j.jpcs.2009.12.063.
[26] H. Sadegh, R. Shahryari-ghoshekandi, M. Kazemi, Study in synthesis and characterization of carbon nanotubes decorated by magnetic iron oxide nanoparticles, Int. Nano Lett. 4 (4) (2014) 129–135, https://doi.org/10.1007/s40089-014-0128-1.
[27] Y. Dai, Y. Xu, D. Jiang, et al., Electromagnetic interference shielding of flexible carboxymethyl cellulose/MWCNT@Fe(3)O(4) composite film with ultralow reflection loss, Int. J. Biol. Macromol. 257 (Pt 1) (Feb 2024) 128604, https://doi.org/10.1016/j.ijbiomac.2023.128604.
[28] Y.-H. Lee, L.-Y. Wang, C.-Y. Tsai, C.-W. Lee, Self-healing nanocomposites with carbon nanotube/graphene/Fe3O4 nanoparticle tricontinuous networks for electromagnetic radiation shielding, ACS Appl. Nano Mater. 5 (11) (2022) 16423–16439, https://doi.org/10.1021/acsanm.2c03492.
[29] E. Thostenson, C. Li, T. Chou, Nanocomposites in context, Compos. Sci. Technol. 65 (3-4) (2005) 491–516, https://doi.org/10.1016/j.compscitech.2004.11.003.
[30] Z. Ali, S. Yaqoob, A. Lo Schiavo, A. D'Amore, Optimizing mechanical and electrical performance of SWCNTs/Fe(3)O(4) epoxy nanocomposites: the role of filler concentration and alignment, Polym. (Basel) 16 (18) (Sep 13 2024), https://doi.org/10.3390/polym16182595.
[31] M.M. Rahman, K.H. Khan, M.M.H. Parvez, N. Irizarry, M.N. Uddin, Polymer nanocomposites with optimized nanoparticle dispersion and enhanced functionalities for industrial applications, Processes 13 (4) (2025), https://doi.org/10.3390/pr13040994.
[32] S. Zhang, Q. An, D. Li, et al., Multifunctional meta-absorber based on CB-PLA composite and magnetic materials for electromagnetic absorption and load-bearing capacity, Compos. Sci. Technol. 264 (May 3 2025) 111131, https://doi.org/10.1016/j.compscitech.2025.111131.
[33] G. Wang, L. Wang, L.H. Mark, et al., Ultralow-threshold and lightweight biodegradable porous PLA/MWCNT with segregated conductive networks for high-performance thermal insulation and electromagnetic interference shielding applications, ACS Appl. Mater. Interfaces 10 (1) (Jan 10 2018) 1195–1203, https://doi.org/10.1021/acsami.7b14111.
[34] T.-B. Ma, H. Ma, K.-P. Ruan, et al., Thermally conductive poly(lactic acid) composites with superior electromagnetic shielding performances via 3D printing technology, Artic. Chin. J. Polym. Sci. 40 (3) (Mar 2022) 248–255, https://doi.org/10.1007/s10118-022-2673-9.
[35] K. Chizari, M. Arjmand, Z. Liu, U. Sundararaj, D. Therriault, Three-dimensional printing of highly conductive polymer nanocomposites for EMI shielding applications, Mater. Today Commun. 11 (Jun 2017) 112–118, https://doi.org/10.1016/j.mtcomm.2017.02.006.
[36] M. Puchalski, G. Szparaga, T. Biela, A. Gutowska, S. Sztajnowski, I. Krucinska, Molecular and Supramolecular Changes in Polybutylene Succinate (PBS) and Polybutylene Succinate Adipate (PBSA) Copolymer during Degradation in Various Environmental Conditions, Polym. (Basel) 10 (3) (Mar 1 2018), https://doi.org/10.3390/polym10030251.
[37] M. Bleija, O. Platnieks, J. Macutkevic, O. Starkova, S. Gaidukovs, Comparison of Carbon-Nanoparticle-Filled Poly(Butylene Succinate-co-Adipate) Nanocomposites for Electromagnetic Applications, 3671, Artic. Nanomater. (Basel) 12 (20) (Oct 19 2022) 17, https://doi.org/10.3390/nano12203671.
[38] H.-J. Tai, Dielectric spectroscopy of poly(butylene succinate) films, Polymer 48 (15) (2007) 4558–4566, https://doi.org/10.1016/j.polymer.2007.05.043.
[39] J. Kruzelak, A. Kvasnicakova, K. Hlozekova, I. Hudec, Progress in polymers and polymer composites used as efficient materials for EMI shielding, Nanoscale Adv. 3 (1) (Jan 7 2021) 123–172, https://doi.org/10.1039/d0na00760a.
[40] A. Nazir, A review of polyvinylidene fluoride (PVDF), polyurethane (PU), and polyaniline (PANI) composites-based materials for electromagnetic interference shielding, J. Thermoplast. Compos. Mater. 35 (10) (2020) 1790–1810, https://doi.org/10.1177/0892705720925120.
[41] A.A. Albert, V. Parthasarathy, P.S. Kumar, Review on recent progress in epoxy-based composite materials for Electromagnetic Interference(EMI) shielding applications, Polym. Compos. 45 (3) (2023) 1956–1984, https://doi.org/10.1002/pc.27928.
[42] R. Massart, Preparation of aqueous magnetic liquids in alkaline and acidic media, Ieee T Magn. 17 (2) (1981) 1247–1248, https://doi.org/10.1109/TMAG.1981.1061188.
[43] J.W. Essam, Percolation theory, Rep. Progress. Phys. 43 (7) (1980) 833–912, https://doi.org/10.1088/0034-4885/43/7/001.
[44] S. Kirkpatrick, Percolation and conduction, Rev. Mod. Phys. 45 (4) (1973) 574–588, https://doi.org/10.1103/RevModPhys.45.574.
[45] P. Potschke, M.H. Arnaldo, H.-J. Radusch, Percolation behavior and mehanical properties of polycarbonate composites filled with carbon black/carbon nanotube systems, Polimery 57 (3) (2012) 204–211, https://doi.org/10.14314/polimery.2012.204.
[46] J. Grigas, Microwave dielectric spectroscopy of ferroelectrics, Ferroelectrics 380 (1) (2009) 113–121, https://doi.org/10.1080/00150190902876249.
[47] L. Cai, Z. Qi, J. Xu, B. Guo, Z. Huang, Study on the photodegradation stability of Poly(butylene Succinate-co-butylene Adipate)/TiO2 nanocomposites, J. Chem. 2019 (2019) 1–9, https://doi.org/10.1155/2019/5036019.
[48] R.D. Cowan, Pulse method of measuring thermal diffusivity at high temperatures, J. Appl. Phys. 34 (4) (1963) 926–927, https://doi.org/10.1063/1.1729564.
[49] F. Zabihi, F. Taleshi, A. Salmani, A. Pahlavan, N. Dehghan-niarostami, M. M. Vadadi, Influence of carbon nanotubes support on the morphology of Fe3O4 nanoparticles, Appl. Nanosci. 5 (3) (2014) 267–272, https://doi.org/10.1007/s13204-014-0314-5.
[50] D.N. Futaba, K. Hata, T. Yamada, et al., Shape-engineerable and highly densely packed single-walled carbon nanotubes and their application as super-capacitor electrodes, Nat. Mater. 5 (12) (2006) 987–994, https://doi.org/10.1038/nmat1782.
[51] P. Soltanpour, R. Naderali, K. Mabhouti, Comparative study on structural, morphological, and optical properties of MS/Fe3O4 nanocomposites and M-doped Fe3O4 nanopowders (M = Mn, Zn), Sci. Rep. 14 (1) (Sep 12 2024) 21287, https://doi.org/10.1038/s41598-024-72026-6.

[52] L. Kumar, P. Kumar, A. Narayan, M. Kar, Rietveld analysis of XRD patterns of different sizes of nanocrystalline cobalt ferrite, Int. Nano Lett. 3 (1) (2013), https://doi.org/10.1186/2228-5326-3-8.
[53] S. Ilyas, Heryanto, B. Abdullah, D. Tahir, X-ray diffraction analysis of nanocomposite Fe3O4/activated carbon by Williamson–Hall and size-strain plot methods, Nano-Struct. & Nano-Objects (2019) 20, https://doi.org/10.1016/j.nanoso.2019.100396.
[54] M.R. Predtechenskiy, A.A. Khasin, A.E. Bezrodny, et al., New perspectives in SWCNT applications: Tuball SWCNTs. Part 1. Tuball by itself—All you need to know about it, Carbon Trends (2022) 8, https://doi.org/10.1016/j.cartre.2022.100175.
[55] J. Ma, C. Liu, Turning waste into treasure: reuse of contaminant-laden adsorbents (Cr(vi)-Fe(3)O(4)/C) as anodes with high potassium-storage capacity, J. Colloid Interface Sci. 582 (Pt B) (Jan 15 2021) 1107–1115, https://doi.org/10.1016/j.jcis.2020.08.110.
[56] Behrendt D.R., Hegland D.E. Saturation Magnetization of Polycrystalline Iron. NASA. https://ntrs.nasa.gov/citations/19720015089.
[57] W. Kiciński, S. Dyjak, Transition metal impurities in carbon-based materials: Pitfalls, artifacts and deleterious effects, Carbon 168 (2020) 748–845, https://doi.org/10.1016/j.carbon.2020.06.004.
[58] Smit J., Wijn H.P.J. *Ferrites*. Meulenhoff; 1959.
[59] J. Baumgartner, L. Bertinetti, M. Widdrat, A.M. Hirt, D. Faivre, Formation of magnetite nanoparticles at low temperature: from superparamagnetic to stable single domain particles, PLoS. One 8 (3) (2013) e57070, https://doi.org/10.1371/journal.pone.0057070.
[60] W. Zhong, P. Liu, Z. Tang, X. Wu, J. Qiu, Facile Approach for Superparamagnetic CNT-Fe3O4/Polystyrene Tricomponent Nanocomposite via Synergetic Dispersion, Ind. & Eng. Chem. Res. 51 (37) (2012) 12017–12024, https://doi.org/10.1021/ie300891h.
[61] M. Narkis, G. Lidor, A. Vaxman, L. Zuri, New injection moldable electrostatic dissipative (ESD) composites based on very low carbon black loadings, J. Electrost. 47 (4) (1999) 201–214, https://doi.org/10.1016/S0304-3886(99)00041-8.
[62] A.K. Jonscher, The 'universal' dielectric response, Nature 267 (5613) (1977) 673–679, https://doi.org/10.1038/267673a0.
[63] A.S. Ushakova, A.A. Lazutin, V.V. Vasilevskaya, Flowerlike Multipetal Structures of Nanoparticles Decorated by Amphiphilic Homopolymers, Macromolecules 54 (13) (2021) 6285–6295, https://doi.org/10.1021/acs.macromol.1c00467.
[64] T. Shiga, Y. Terada, S. Chiashi, T. Kodama, Effect of bundling on phonon transport in single-walled carbon nanotubes, Carbon (2024) 223, https://doi.org/10.1016/j.carbon.2024.119048.
[65] S.A. Schelkunoff, A mathematical theory of linear arrays, Bell Syst. Tech. J. 22 (1) (1943) 80–107, https://doi.org/10.1002/j.1538-7305.1943.tb01306.x.
[66] P. Saini, M. Arora, Microwave absorption and EMI shielding behavior of nanocomposites based on intrinsically conducting polymers, graphene and carbon nanotubes, New. Polym. Spec. Appl. (2012) 71–112, https://doi.org/10.5772/48779.
[67] A. Ameli, M. Nofar, C.B. Park, P. Pötschke, G. Rizvi, Polypropylene/carbon nanotube nano/microcellular structures with high dielectric permittivity, low dielectric loss, and low percolation threshold, Carbon 71 (2014) 206–217, https://doi.org/10.1016/j.carbon.2014.01.031.
[68] M. Cao, R. Qin, C. Qiu, J. Zhu, Matching design and mismatching analysis towards radar absorbing coatings based on conducting plate, Mater. Des. 24 (5) (2003) 391–396, https://doi.org/10.1016/S0261-3069(02)00119-X.
[69] R.C. Che, L.M. Peng, X.F. Duan, Q. Chen, X.L. Liang, Microwave absorption enhancement and complex permittivity and permeability of Fe encapsulated within carbon nanotubes, Adv. Mater. 16 (5) (2004) 401–405, https://doi.org/10.1002/adma.200306460.
[70] Y. Danlée, F. Mederos-Henry, S. Hermans, C. Bailly, I. Huynen, Ranking broadband microwave absorption performance of multilayered polymer nanocomposites containing carbon and metallic nanofillers, Front. Mater. (2020) 7, https://doi.org/10.3389/fmats.2020.00214.
[71] G. Tian, H. He, M. Xu, Y. Liu, Q. Gao, Z. Zhu, Ultralow percolation threshold biodegradable PLA/PBS/MWCNTs with segregated conductive networks for high-performance electromagnetic interference shielding applications. Article, J. Appl. Polym. Sci. 140 (9) (Mar 2022) 12, https://doi.org/10.1002/app.53558.
[72] C.Y. Cheng, Q.H. Pho, X.Y. Wu, et al., PLGA Microspheres Loaded with beta-Cyclodextrin Complexes of Epigallocatechin-3-Gallate for the Anti-Inflammatory Properties in Activated Microglial Cells, Polym. (Basel) 10 (5) (May 11 2018), https://doi.org/10.3390/polym10050519.
[73] V. Sivanjineyulu, K. Behera, Y.-H. Chang, F.-C. Chiu, Selective localization of carbon nanotube and organoclay in biodegradable poly(butylene succinate)/polylactide blend-based nanocomposites with enhanced rigidity, toughness and electrical conductivity, Compos. Part A Appl. Sci. Manufacturing 114 (2018) 30–39, https://doi.org/10.1016/j.compositesa.2018.08.009.
[74] A.J. Müller, M.L. Arnal, M. Trujillo, A.T. Lorenzo, Super-nucleation in nanocomposites and confinement effects on the crystallizable components within block copolymers, miktoarm star copolymers and nanocomposites, Eur. Polym. J. 47 (4) (2011) 614–629, https://doi.org/10.1016/j.eurpolymj.2010.09.027.
[75] J.Y. Luo, D.X. Yin, K.J. Yu, H.F. Zhou, B.Y. Wen, X.D. Wang, Facile Fabrication of PBS/CNTs Nanocomposite Foam for Electromagnetic Interference Shielding, Artic. ChemPhysChem. 23 (4) (Feb 2022) 12, https://doi.org/10.1002/cphc.202100778.
[76] T.P. Gumede, A.S. Luyt, A.J. Muller, Review on PCL, PBS, and PCL/PBS blends containing carbon nanotubes, Express Polym. Lett. 12 (6) (2018) 505–529, https://doi.org/10.3144/expresspolymlett.2018.43.
[77] A.M. Gohn, J. Seo, R.H. Colby, R.P. Schaake, R. Androsch, A.M. Rhoades, Crystal nucleation in poly(ether ether ketone)/carbon nanotube nanocomposites at high and low supercooling of the melt, Polymer (2020) 199, https://doi.org/10.1016/j.polymer.2020.122548.
[78] Y. Wang, L. Fang, C. Xu, Z. Chen, Y. Chen, Preparation and properties of dynamically cured poly(vinylidene fluoride)/silicone rubber blends, Polym. Test. 32 (6) (2013) 1072–1078, https://doi.org/10.1016/j.polymertesting.2013.06.007.
[79] L. Bai, X. Zhao, R.-Y. Bao, Z.-Y. Liu, M.-B. Yang, W. Yang, Effect of temperature, crystallinity and molecular chain orientation on the thermal conductivity of polymers: a case study of PLLA, J. Mater. Sci. 53 (14) (2018) 10543–10553, https://doi.org/10.1007/s10853-018-2306-4.
[80] C. Huang, X. Qian, R. Yang, Thermal conductivity of polymers and polymer nanocomposites, Mat. Sci. Eng. R. 132 (2018) 1–22, https://doi.org/10.1016/j.mser.2018.06.002.
[81] E. Pop, D. Mann, Q. Wang, K. Goodson, H. Dai, Thermal conductance of an individual single-wall carbon nanotube above room temperature, Nano Lett. 6 (1) (Jan 2006) 96–100, https://doi.org/10.1021/nl052145f.
[82] P. Kim, L. Shi, A. Majumdar, P.L. McEuen, Thermal transport measurements of individual multiwalled nanotubes, Phys. Rev. Lett. 87 (21) (Nov 19 2001) 215502, https://doi.org/10.1103/PhysRevLett.87.215502.
[83] S. Berber, Y.K. Kwon, D. Tomanek, Unusually high thermal conductivity of carbon nanotubes, Phys. Rev. Lett. 84 (20) (May 15 2000) 4613–4616, https://doi.org/10.1103/PhysRevLett.84.4613.
[84] J. Yang, S. Waltermire, Y. Chen, A.A. Zinn, T.T. Xu, D. Li, Contact thermal resistance between individual multiwall carbon nanotubes, Appl. Phys. Lett. 96 (2) (2010), https://doi.org/10.1063/1.3292203.
[85] Y. Gao, Y. Shao, L. Yan, et al., Efficient charge injection in organic field-effect transistors enabled by low-temperature atomic layer deposition of ultrathin VOx interlayer, Adv. Funct. Mater. 26 (25) (2016) 4456–4463, https://doi.org/10.1002/adfm.201600482.
[86] Q. Wang, Y. Zhang, Y. Li, et al., A new perspective on the needle-puncture property of silkworm cocoons with a hierarchical multi-layer structure, Compos. Commun. 22 (2020), https://doi.org/10.1016/j.coco.2020.100539.
[87] Z. Wang, Z. Wu, L. Weng, et al., A roadmap review of thermally conductive polymer composites: critical factors, progress, and prospects, Adv. Funct. Mater. 33 (36) (2023), https://doi.org/10.1002/adfm.202301549.
[88] Y. Su, J.J. Li, G.J. Weng, Theory of thermal conductivity of graphene-polymer nanocomposites with interfacial Kapitza resistance and graphene-graphene contact resistance, Carbon 137 (2018) 222–233, https://doi.org/10.1016/j.carbon.2018.05.033.
[89] O.A. Bârsan, G.G. Hoffmann, L.G.J. van der Ven, G. de With, Single-walled carbon nanotube networks: the influence of individual tube–tube contacts on the large-scale conductivity of polymer composites, Adv. Funct. Mater. 26 (24) (2016) 4377–4385, https://doi.org/10.1002/adfm.201600435.
[90] E. Tarani, K. Pušnik Črešnar, L.F. Zemljič, et al., Cold crystallization kinetics and thermal degradation of PLA composites with metal oxide nanofillers, Appl. Sci. 11 (7) (2021), https://doi.org/10.3390/app11073004.
[91] C.R. Ferreira, C.V. Santilli, V. Briois, S.H. Pulcinelli, Relevance of the iron distribution in natural smectite clays for the thermal stability of PMMA-clay nanocomposites, ACS Omega 9 (34) (Aug 27 2024) 36579–36588, https://doi.org/10.1021/acsomega.4c04751.
[92] F. Pincella, K. Isozaki, R. Sato, T. Teranishi, H. Takaya, M. Nakamura, Reusable magnetite nanoparticle (Fe(3)O(4) NP) catalyst for selective oxidation of alcohols under microwave irradiation, ACS Omega 9 (23) (Jun 11 2024) 24477–24488, https://doi.org/10.1021/acsomega.4c00361.
[93] F. Du, R.C. Scogna, W. Zhou, S. Brand, J.E. Fischer, K.I. Winey, Nanotube networks in polymer nanocomposites: rheology and electrical conductivity, Macromolecules 37 (24) (2004) 9048–9055, https://doi.org/10.1021/ma049164g.
[94] P. Pötschke, T.D. Fornes, D.R. Paul, Rheological behavior of multiwalled carbon nanotube/polycarbonate composites, Polymer 43 (11) (2002) 3247–3255, https://doi.org/10.1016/S0032-3861(02)00151-9.
[95] N. Bagotia, D.K. Sharma, Systematic study of dynamic mechanical and thermal properties of multiwalled carbon nanotube reinforced polycarbonate/ethylene methyl acrylate nanocomposites, Polym. Test. 73 (2019) 425–432, https://doi.org/10.1016/j.polymertesting.2018.12.006.
[96] J.N. Coleman, U. Khan, Y.K. Gun'ko, Mechanical reinforcement of polymers using carbon nanotubes, Adv. Mater. 18 (6) (2006) 689–706, https://doi.org/10.1002/adma.200501851.
[97] P. Rodriguez, Serrated plastic flow, Bull. Mater. Sci. 6 (4) (1984) 653–663, https://doi.org/10.1007/BF02743993.